

**InGaAs/GaAs/InGaP
980nm LASERS**

**GROWTH OPTIMIZATION AND FABRICATION
OF 980nm InGaAs/GaAs/InGaP LASERS**

By
Tullio Panarello

A Thesis
Submitted to the School of Graduate Studies
in Partial Fulfillment of the Requirements
for the Degree
Master of Engineering

McMaster University
Hamilton, Ontario
Canada

MASTER OF ENGINEERING (1997)
(Engineering Physics)

McMASTER UNIVERSITY
Hamilton, Ontario

TITLE: Growth Optimization and Fabrication of 980nm InGaAs/GaAs/InGaP
Lasers

AUTHOR: Tullio Panarello, B.Sc. (Concordia University)

SUPERVISORS: Dr. D.A. Thompson
Dr. J.G. Simmons

NUMBER OF PAGES: viii, 60

ABSTRACT

The growth optimization and fabrication of 980nm quantum well (QW) lasers is presented. Photoluminescence (PL) spectroscopy is used to determine the optimized growth conditions for the QWs. The results are presented for optimization of both growth temperature and group V overpressure. Broad area lasers, with active regions grown at and around optimized QW growth conditions, are fabricated and characterized under pulsed conditions. These results are used to determine the optimum growth conditions for a ridge waveguide (RWG) laser structure. Once grown, RWG lasers are fabricated and characterized under continuous wave (CW) conditions. External quantum efficiencies as high as 71 % and cavity losses as low as 5.2 cm^{-1} are achieved.

ACKNOWLEDGMENTS

I wish to express my sincere appreciation to my supervisors, Dr. Dave Thompson and Dr. John Simmons for their support, direction, and advice during the course of my graduate studies. I would also like to thank Brad Robinson for his guidance and instruction in all matters relating to MBE and fine Scotches.

The work presented in this thesis could not have proceeded without the help and continuing support of three outstanding fellow graduate students: Eugene Tan, Jim Swoger and Ray Lapierre. To these three gentlemen I express my most sincere thanks and gratitude for their help with fabrication, device characterization, PL and X-ray. I hope I was not too much of a burden.

A very special thanks goes out to Jeff Brown. He was a friend, when real friends were hard to come by, he kept me sane, and never allowed me to quit. He has probably read this thesis as many times as I have. I would also like to thank Michael Ersoni for his support and his company on those long drives back and forth from Montreal.

Finally and most importantly, I am very grateful to my wife Sotiria Pischos and to my parents Sabatino and Alessandra Panarello for their love, encouragement and support.

TABLE OF CONTENTS

1.0 INTRODUCTION	1
1.1 Motivation and Background.....	1
1.2 Quantum Well Lasers.....	4
1.2.1 InGaP-InGaAs-GaAs 980nm Lasers.....	9
1.3 Semiconductor Growth Via Molecular Beam Epitaxy.....	10
1.3.1 Gas Source Molecular Beam Epitaxy.....	10
1.3.2 Thermodynamics and Kinetics of Crystal Growth.....	12
1.3.3 McMaster Gas Source Molecular Beam Epitaxy.....	15
2.0 CHARACTERIZATION TECHNIQUES	18
2.1 Introduction.....	18
2.2 Photoluminescence.....	18
2.2.1 Theory.....	19
2.2.2 Transition Characteristics.....	23
2.2.3 Experimental Setup.....	27
2.3 Laser Characterization.....	28
3.0 LASER FABRICATION	31
3.1 Introduction.....	31
3.2 Sample Cleaning.....	31
3.3 Photolithography.....	33
3.4 Laser Processing.....	36
4.0 OPTIMIZATION RESULTS	39
4.1 Introduction.....	39
4.2 QW Optimization.....	40
4.3 Broad Area Lasers.....	45
4.4 RWG Lasers.....	49
5.0 CONCLUSION	56
REFERENCES	58

LIST OF FIGURES

Figure 1.1:	Energy level scheme for Er^{+3} ions in EDFA [1.3].	2
Figure 1.2:	Minimum bandgap versus lattice constant data for III-V, II-VI and group IV semiconductors [1.8].	4
Figure 1.3:	Bulk bandgap energy for strained and unstrained $\text{In}_x\text{Ga}_{1-x}\text{As}$ on GaAs [1.13].	
Figure 1.4:	Schematic diagram of energy levels in a QW.	7
Figure 1.5:	Equilibrium partial pressures of As , As_2 , and As_4 as a function of total pressure of the arsenic species at different cracker temperatures [1.21].	11
Figure 1.6:	Surface interaction potential for a physisorbed and chemisorbed states [1.23].	13
Figure 1.7:	Plot of the vapor pressures of As over As rich GaAs ($P_{\text{As}/\text{As rich}}$), As over Ga rich GaAs ($P_{\text{As}/\text{Ga rich}}$), Ga over As rich GaAs ($P_{\text{Ga}/\text{As rich}}$), and Ga over Ga rich GaAs ($P_{\text{Ga}/\text{Ga rich}}$) [1.24].	14
Figure 1.8:	Schematic of the McMaster GS-MBE [1.25]	16
Figure 2.1:	Fermi level for a) semiconductor in equilibrium state and b) semiconductor not in equilibrium state [2.3].	21
Figure 2.2:	Graph of intensity vs emitted photon energy for an arbitrary semiconductor with 1 eV bandgap energy.	22
Figure 2.3:	Shape of PL emission for QW with smooth (a) and rough (b) interface [2.10].	26
Figure 2.4:	PL spectroscopy setup	27
Figure 2.5:	P-I plot for 50x300 mm broad area laser showing the threshold current and determination of external quantum efficiency.	29

Figure 3.1:	Resist profiles for (a) etch mask process and (b) liftoff mask process.	35
Figure 3.2:	Ridge waveguide laser process flow: (a) Structure outline, (b) Etched ridge, (c) Silicon dioxide passivated ridge with open contact area on ridge, and (d) Finished RWG laser with p- and n-type metal contacts.	37
Figure 4.1:	Pulsed P-I plot of 30 μ m strip broad area laser (0.2 μ s pulse width and 1 % duty cycle).	39
Figure 4.2:	Sample QW structure for growth optimization studies.	41
Figure 4.3:	PL spectra at 11 K of QW samples in the growth temperature study.	41
Figure 4.4:	PL spectra at 11K of samples in the group V flow rate study.	44
Figure 4.5:	Structure grown for broad area laser study.	46
Figure 4.6:	Typical pulsed P-I plots for 50x500 μ m broad area lasers.	47
Figure 4.7:	Comparative analysis of 50 μ m strip broad area lasers: (a) threshold current vs cavity length, (b) external quantum efficiency vs cavity length.	48
Figure 4.8:	Layer structure for ridge waveguide laser.	50
Figure 4.9:	Typical CW P-I plots for 2 μ m ridge waveguide lasers with 500, 750, 1000, and 1500 μ m cavity lengths.	51
Figure 4.10:	Analysis of 2 and 4 μ m ridge waveguide lasers: (a) threshold current vs cavity length, (b) inverse external quantum efficiency vs cavity length.	52
Figure 4.11:	PL spectra of ridge waveguide laser structure.	53
Figure 4.12:	Structure for the interface gas swap study.	54
Figure 4.13:	PL spectra of the defect peaks for the interface study	55

LIST OF TABLES

Table 1.1:	Material parameters for InAs and GaAs [1.14].	6
Table 2.1:	Semiconductor properties which can be characterized by the following optical methods: photoluminescence (PL), Raman spectroscopy (Raman) and infrared absorption spectroscopy (IR) [2.1].	19
Table 3.1:	Organic solvents used for sample cleaning.	32
Table 4.1:	QW growth parameters for the growth temperature optimization study.	42
Table 4.2:	QW growth parameters for group V flow rate study.	43
Table 4.3:	QW growth conditions for broad area laser study.	46
Table 4.4:	Summary of broad area laser results.	49
Table 4.5:	Internal quantum efficiency and cavity loss for 2 and 4 μ m RWG lasers.	51
Table 4.6:	Gas swap delay times for interface study.	54

1.0 INTRODUCTION

1.1 Motivation and Background

The recent increased demand for advanced telecommunication services has given rise to tremendous technological progress in the field of communications via optical transmission. Today, systems that operate at bit rates of 1.2-2.4 Gb/s are available as commercial units, while systems which operate at 20-40 Gb/s have already been demonstrated in the laboratory [1.1]. These transmission rates have been made possible by the use of active fiber devices. These devices eliminate the high speed, electronic based, optical receiver/transmitter units required to overcome signal degradation over long hauls. One such system is the Erbium-doped fiber amplifier (EDFA) which provides a means of all optical compensation of intrinsic fiber losses. Amplification via EDFA does not require detection, regeneration and retransmission of the incoming optical signal. Furthermore, EDFAs are bit rate independent [1.2], and therefore need not be replaced when systems are upgraded.

An EDFA consists of a short length of optical fiber, the core of which has been doped with approximately 0.1% Er. When photons with energy corresponding to a transition from the Er ion ground state to an excited state pass through this doped length of fiber (called the active region), they are absorbed by the ions. This excited state is referred to as the "pump band" (see Figure 1.1 for energy level diagram [1.3]). Once in

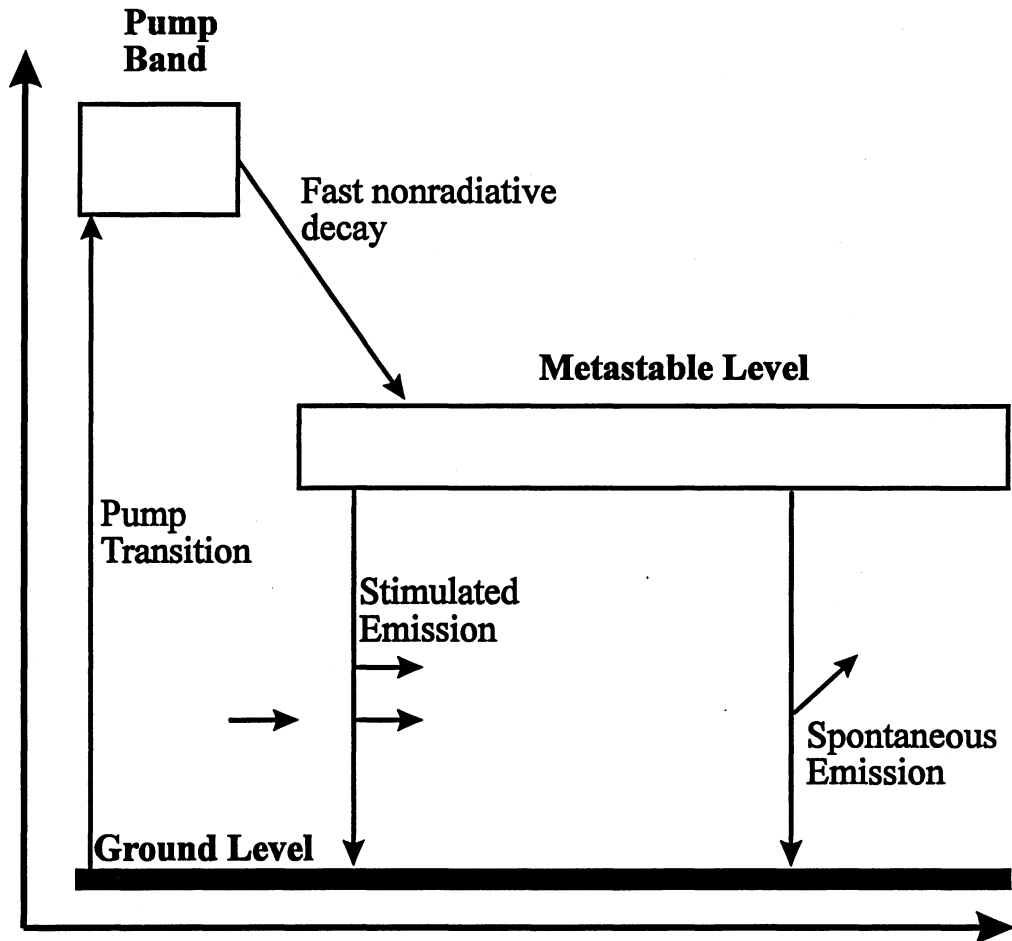


Fig. 1.1. Energy level scheme for Er^{3+} ions in EDFA [1.3].

the pump band, the ions undergo a fast nonradiative decay to a metastable level. This metastable level is separated from the ground state by an energy gap corresponding to the $1.55 \mu\text{m}$ emission wavelength used in telecommunications. It is further characterized by a long spontaneous emission lifetime of 10 ms. The level acts as a bottleneck in the cascade of excited ions toward the ground state, allowing the formation of a population inversion for a sufficiently large optical pumping intensity. Signal photons, with wavelengths of about $1.55 \mu\text{m}$, which pass through the active region will therefore stimulate the depopulation of the metastable level thus amplifying the signal.

EDFAs can be pumped with 1480 or 980 nm lasers. Light at 1480 nm excite ions directly to the metastable state, while 980 nm causes excitation through the higher energy pump band. Currently, 1480 nm pump lasers are widely used in commercial systems due to their availability. However, the shorter wavelength 980 nm laser has many advantages over those at 1480 nm. The 980 nm laser has lower threshold current density [1.4], higher differential quantum efficiency [1.5], higher power output and reduced temperature sensitivity [1.6]. Hence they require less electrical power and cooling. Furthermore, EDFA employing 980 nm pump lasers also have a lower noise figure (close to the 3 dB quantum limit) than similar 1480 nm pumped EDFA [1.7]. It is believed that desired increases in communication rates will require the use of EDFA systems employing 980 nm lasers. This obviously requires increased development of the 980 nm laser.

This thesis outlines the growth optimization and fabrication of 980 nm InGaP-InGaAs-GaAs ridge-waveguide QW lasers suitable for use in EDFA systems. This introductory chapter will provide the necessary background in both the fundamentals of laser theory and materials growth by Gas Source-Molecular Beam Epitaxy (GS-MBE). Chapter Two contains an overview of the techniques used to characterize the as grown material and the processed devices. The fabrication methods for both broad area and ridge waveguide structures are outlined in Chapter Three. Experimental results of the material optimization and laser processing are presented in Chapter Four. Finally, the conclusions will be summarized in Chapter Five as well as suggestions for future work.

1.2 Quantum Well Lasers

The two most common semiconductor laser material systems are the naturally lattice matched AlGaAs-GaAs system and the lattice matched InGaAsP-InP system. Using these materials, double heterostructure and quantum well lasers can be grown and fabricated with emission wavelengths ranging from 650 to 880 nm and 1100 to 1600 nm respectively. In order to achieve lasing wavelengths between 880 and 1100 nm a different system is needed. A simple examination of the available direct gap compound semiconductor alloys, shown in Figure 1.2, suggests that wavelengths in this range can be obtained using the InGaAs system. Since InGaAs has a larger lattice constant than the GaAs substrate on which it will be grown, the resulting layer will be strained.

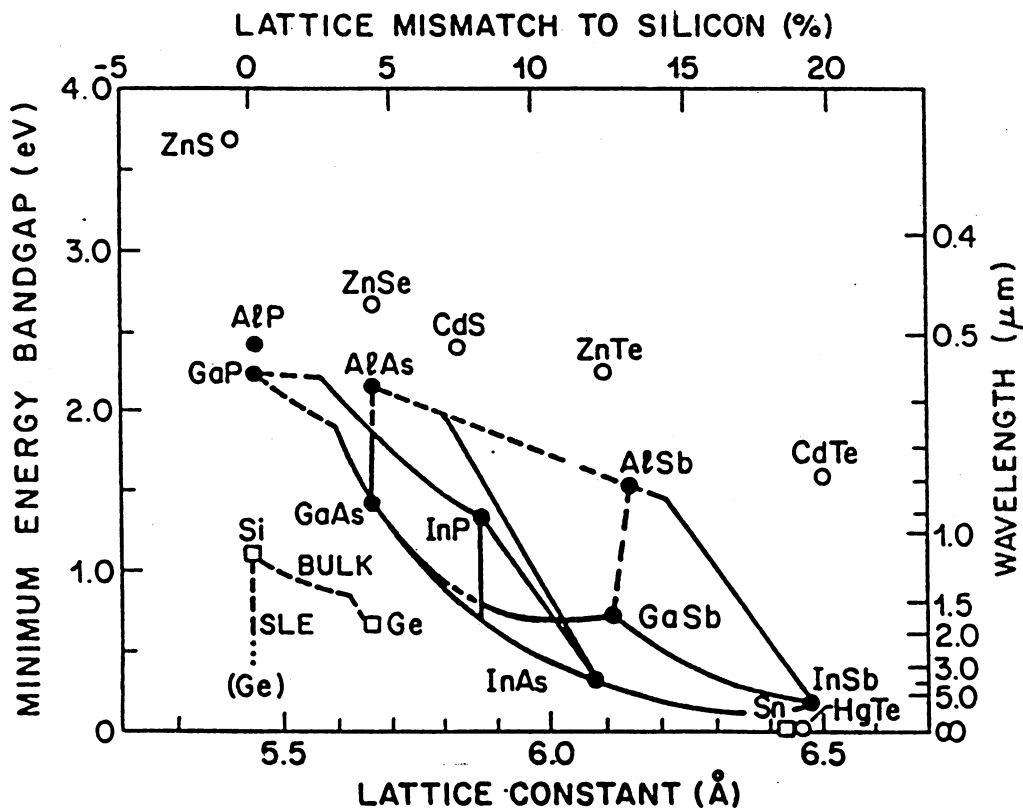


Fig. 1.2 Minimum bandgap versus lattice constant data for III-V, II-VI and group IV semiconductors [1.8].

When designing semiconductor lasers in a latticed matched system, there is no limit on the number or the thickness of the grown layers. In a strained layer system, however, elastic accommodation of the strain energy without the formation of dislocations is a requirement for device applications. The maximum thickness of a strained layer before the strain energy can no longer be accommodated is called the critical thickness (h_c). For different amounts of strain (i.e. lattice mismatch), h_c can be calculated from the Matthews and Blakeslee model [1.9]:

$$h_c = \frac{a}{\kappa\sqrt{2\pi f}} \frac{1-0.25\nu}{1+\nu} \left(\ln \frac{h_c\sqrt{2}}{a} + 1 \right) \quad (1.1)$$

where a is the lattice constant of the substrate. The lattice mismatch, f , is defined as:

$$f = \frac{\Delta a}{a} \quad (1.2)$$

where Δa is the difference in lattice constants. Finally, ν is Poisson's ratio defined as

$$\nu = \frac{C_{12}}{C_{11} + C_{12}} \quad (1.3)$$

where C_{ij} are the elastic stiffness coefficients. The coefficient κ in Eq. 1.1 has a value of 1 for a strained layer superlattice, 2 for a single quantum well and 4 for a single strained layer (i.e. an uncapped strained layer). The limit imposed on the thickness of strained InGaAs layers in InGaAs/GaAs heterostructures restricts the use of InGaAs to QW structures.

A consequence of adding strain to a semiconductor system is the altering of the conduction-band and valence-band energies [1.10-12]. In the strained InGaAs-GaAs

heterostructure system, the presence of biaxial compressive strain alters the cubic symmetry of the zincblende semiconductor lattice. This effect increases the band gap energy and removes the degeneracy of the heavy-hole and light-hole valence bands. The change in energy between the conduction and the valence-band, due to strain is given by [1.13]:

$$\Delta E_{hh} = -2\Xi f \left(\frac{C_{11} - C_{12}}{C_{11}} \right)_{Hydrostatic} + bf \left(\frac{C_{11} + 2C_{12}}{C_{11}} \right)_{shear} \quad (1.4)$$

$$\Delta E_{lh} = -2\Xi f \left(\frac{C_{11} - C_{12}}{C_{11}} \right)_{Hydrostatic} - bf \left(\frac{C_{11} + 2C_{12}}{C_{11}} \right)_{shear} \quad (1.5)$$

where ΔE_{hh} and ΔE_{lh} are the shifts in the heavy and light-hole valence-band edges with respect to the conduction band, and b and Ξ are the shear and hydrostatic deformation potentials. Values for the material parameters needed to calculate the above energy shifts for InGaAs can be interpolated using Vegard's principal from the parameter list in Table 1.1 for InAs and GaAs. Figure 1.3 shows the resulting calculated bulk bandgap energy for both the strained and unstrained InGaAs as a function of In composition.

		InAs	GaAs
Lattice constant (Å)	a_o	6.0585	5.6535
Elastic coefficient (10^{12} dynes/cm ²)	C_{11}	0.865	0.538
	C_{12}	0.485	1.188
Hydrostatic deformation potential (eV)	Ξ	-6.0	-8.2
Shear deformation potential (eV)	b	-1.8	-2.0
Electron effective mass	m_e	0.023	.069
Heavy-Hole effective mass	m_{hh}	0.41	0.47
Light-Hole effective mass	m_{lh}	0.027	0.074
Bandgap (eV)	E_g	0.36	1.42

Table 1.1: Material parameters for InAs and GaAs [1.14].

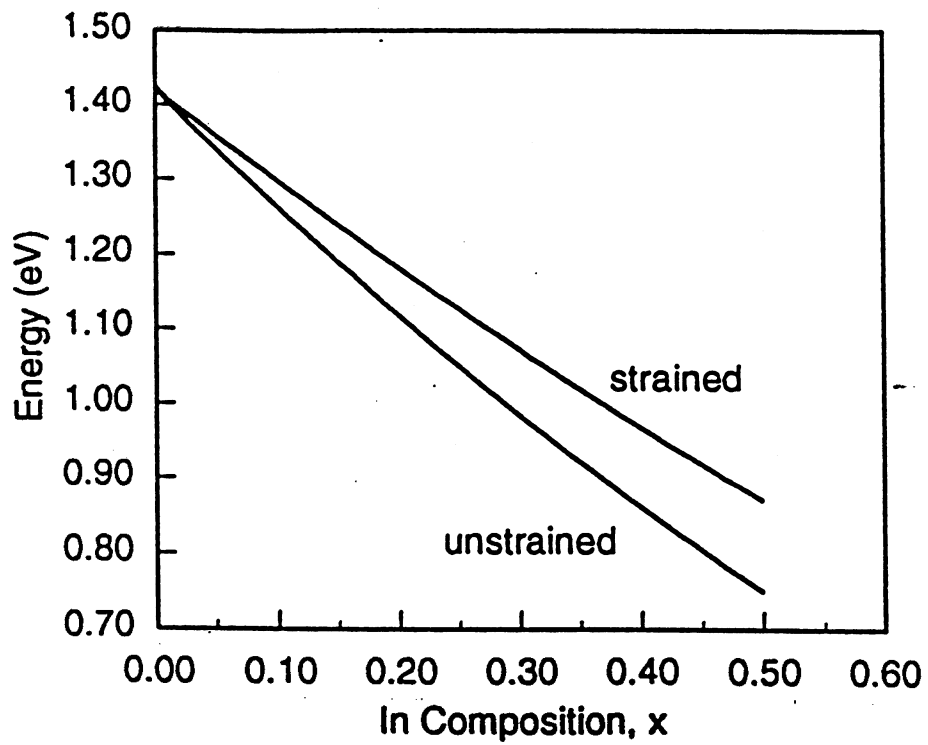


Fig. 1.3: Bulk bandgap energy for strained and unstrained $\text{In}_x\text{Ga}_{1-x}\text{As}$ on GaAs [1.13].

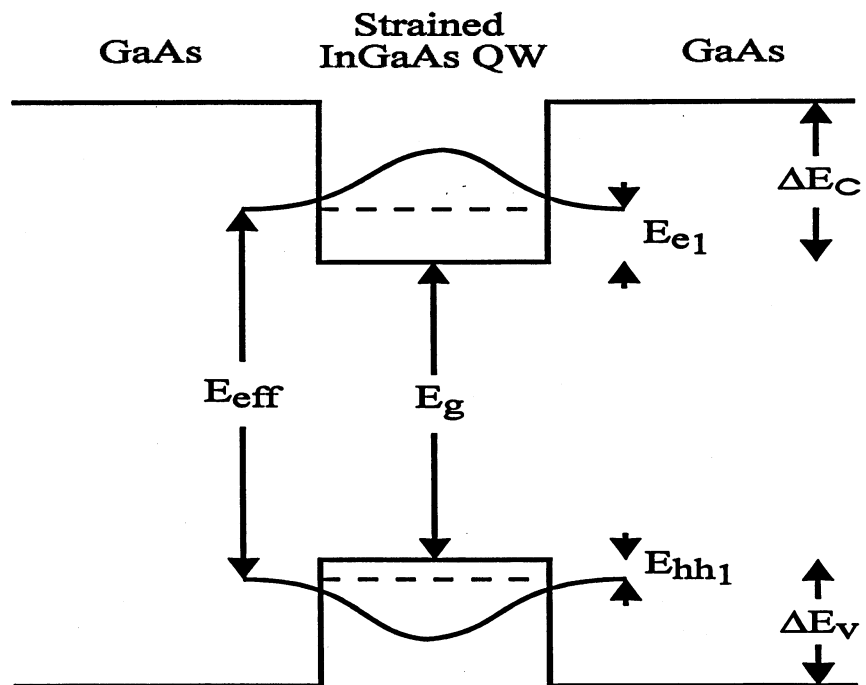


Fig. 1.4: Schematic diagram of energy levels in a QW.

In addition to the change in band-gap energy resulting from strain, quantum size effects will result in the formation of discrete energy bands within the QW, as shown in Figure 1.4. The energy (E_{hh_n} in the valance band and E_{e_n} in the conduction band for $n = 1, 2, 3, \dots$) shifts due to quantization are determined by solving the transcendental equations [1.15]:

$$\text{Tan} \sqrt{\frac{m_w E_{hh_n, e_n} L_z^2}{2(\hbar/2\pi)^2}} = \sqrt{\frac{m_w (\Delta E_{c,v} - E_{hh_n, e_n})}{m_b E_{hh_n, e_n}}} \quad \text{for } n = \text{odd} \quad (1.6)$$

$$\text{Cotan} \sqrt{\frac{m_w E_{hh_n, e_n} L_z^2}{2(\hbar/2\pi)^2}} = -\sqrt{\frac{m_w (\Delta E_{c,v} - E_{hh_n, e_n})}{m_b E_{hh_n, e_n}}} \quad \text{for } n = \text{even} \quad (1.7)$$

where m_w and m_b are the electron (or hole) masses in the well and barrier respectively, $\Delta E_{c,v}$ is the conduction or valance band offset and L_z is the width of the well. Here, the energy shifts E_{hh_n} and E_{e_n} are given by the n^{th} solutions to the above transcendental equations and represent the energy levels in the valance and conduction band of the quantum well. The radiative transition will always occur between the lowest energy bands (i.e. $n=1$ bands) in a semiconductor laser. Taking these various effects into account the transition wavelength for a strained InGaAs QW is given by:

$$\lambda = \frac{hc}{E_g + \Delta E_{hh} + E_{hh_1} + E_{e_1}} \quad (1.8)$$

where E_g is the unstrained InGaAs band gap and ΔE_{hh} , E_{hh_1} and E_{e_1} can be calculated from Eq.'s 1.4 and 1.6.

1.2.1 InGaP-InGaAs-GaAs 980 nm Lasers

Most 980 nm lasers in use today incorporate AlGaAs cladding layers. This high bandgap, low refractive index material (relative to the InGaAs-GaAs active region), provides the both the carrier and optical confinement needed for good laser performance. Unfortunately, the high aluminum content (about 40 - 60%) in the cladding introduces reliability problems. Catastrophic optical damage (COD) due to facet oxidation, and the formation and propagation of dark line defects limit the lifetimes of these lasers to about 2×10^5 hours [1.16]. This is five times less than that required for reliable subsea transmission cables.

To overcome the reliability problems resulting from Al contained in the cladding region many producers of 980 nm lasers have begun to study InGaP as a replacement for AlGaAs. InGaP lattice matched to GaAs is equal in bandgap energy, to AlGaAs with 40% Al. This new material has many advantages over its AlGaAs: the absence of Al removes the problems of degradation of facets or exposed surfaces due to oxidation [1.17]; the availability of selective etches between InGaP and GaAs (nonexistent for AlGaAs/GaAs) results in good control of laser stripe definition; InGaP's high resistance to the formation and spread of dark line defects [1.18]; and finally the ability of uncoated facets to sustain higher optical power densities before COD [1.19] results in higher reliability.

1.3 Semiconductor Growth Via Molecular Beam Epitaxy

Molecular Beam Epitaxy (MBE) may be described as a sophisticated evaporation technique performed in ultra high vacuum. The substrate is placed in high vacuum and beams of elemental species impinge on the surface of the heated substrate. At the surface, the species assemble into a crystalline order as a continuation of the substrate. With proper control of the elemental species (example: Ga, In, As, P, Be and Si) almost any material composition and doping can be achieved. MBE also provides excellent control of layer thickness, virtually on the order of one atomic layer.

1.3.1 Gas Source Molecular Beam Epitaxy

Various techniques exist for MBE growth classified by the method in which the elemental beams are created. In solid source MBE (SSMBE) all elemental species are provided through the evaporation of solids in effusion cells. The evaporation rate of the solid, and therefore the beam intensity, are controlled by the cell temperature. The heated material vaporizes and exits the cell. The low background pressure (below 10^{-9} Torr) and small pressure produced by the particle flux (beam equivalent pressures of 10^{-6} to 10^{-4} Torr) allow the production of a molecular beam which will travel from the source to the substrate without interaction. Supply of the material is controlled by a mechanical shutter located near the opening of the effusion cell which interrupts the beam. While this technique is suitable for the growth of many semiconductor compounds, it is generally not suited for the production of phosphorous containing materials. Precise control of the intensity of the phosphorous beam is difficult due to the presence of allotropic forms of

phosphorous with different vapour pressures. Furthermore, the predominant vaporization species is P_4 , which has a low accommodation coefficient on the growing crystal surface [1.20]. This tetramer can be reduced to the preferred dimer, P_2 , through the use of a combined effusion and cracking cell. However, this complicates control of the beam intensity.

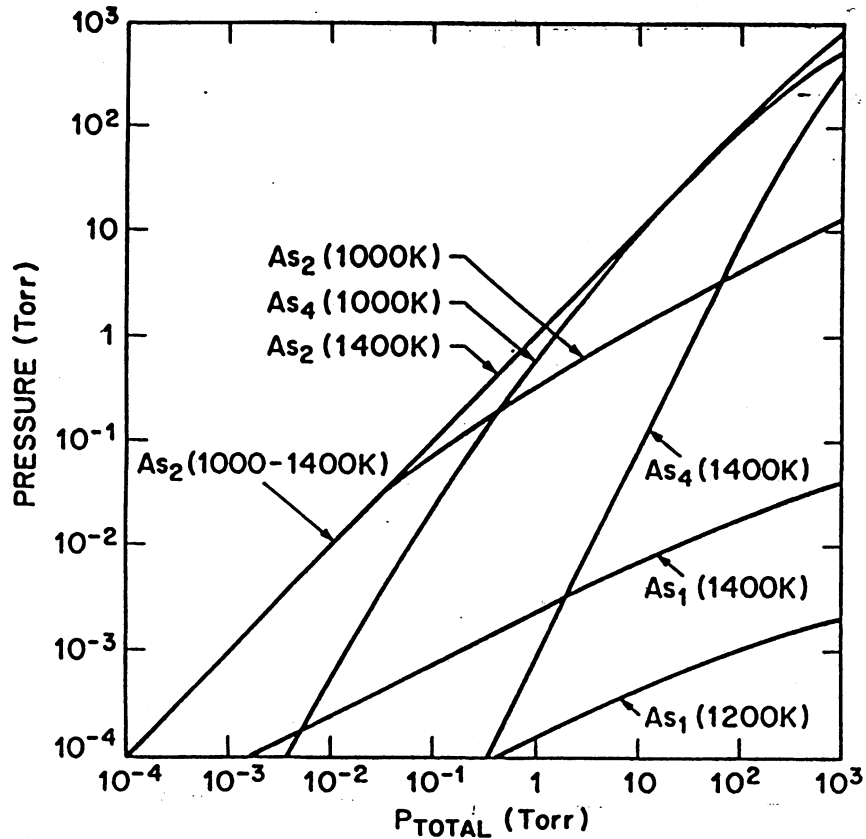


Fig. 1.5: Equilibrium partial pressures of As, As_2 , and As_4 as a function of total pressure of the arsenic species at different cracker temperatures [1.21].

To overcome this impediment in the production of phosphorous containing semiconductors, it is common to supply the elemental group V beams from gaseous species. In gas source MBE (GSMBE), the As_2 and P_2 fluxes are supplied from the thermal decomposition of their respective hydrides: arsine (AsH_3) and phosphine (PH_3). The group III elements are still provided from evaporation of the solid. Thermal

decomposition occurs in the gas cracking cell where a heated rhenium wire catalyses the decomposition of AsH₃ and PH₃. Ideally the decomposition occurs via the reactions:



However, the product of the decomposition can be a mixture of monomers, dimers, and tetramers. The dominant species being produced will depend on the cracker temperature and pressure as seen in Figure 1.5 for As. Given the typical pressure in the cracker is about 10^{-3} Torr for normal growth rates [1.21] and 1000°C cracker temperature, dimers are the predominant species emitted. In GSMBE systems, the hydride sources are mixed in the cracking cell and the cracked products are allowed to effuse into the growth chamber. Unlike the shutter and temperature based control system used for the solid sources, the As₂ and P₂ beams are controlled by a complex gas handling system which is used to set the flow of arsine and phosphine to the cracker cell.

1.3.2 Thermodynamics and Kinetics of Crystal Growth

Atoms which adsorb on the surface of the growing crystal can be bound via one of two processes: physisorption and chemisorption [1.22,23]. In the first process, physisorption, the atom is held to the surface of the growing crystal by Van Der Waal type attractive forces. In this state no electron exchange occurs with the crystal surface, hence these atoms have high surface mobility and large evaporation rates. Chemisorption is characterized by the formation of covalent bonds between the atom and the crystal surface, which makes this a lower energy state compared to physisorption (see Figure

1.6). Atoms on the surface in the physisorbed state must eventually become chemisorbed if they are to be incorporated into the growing crystal. Chemisorbed atoms can still migrate over the crystal surface, but will have a lower desorption rate due to the larger binding energy. Therefore, chemisorbed atoms can be incorporated into the growing crystal.

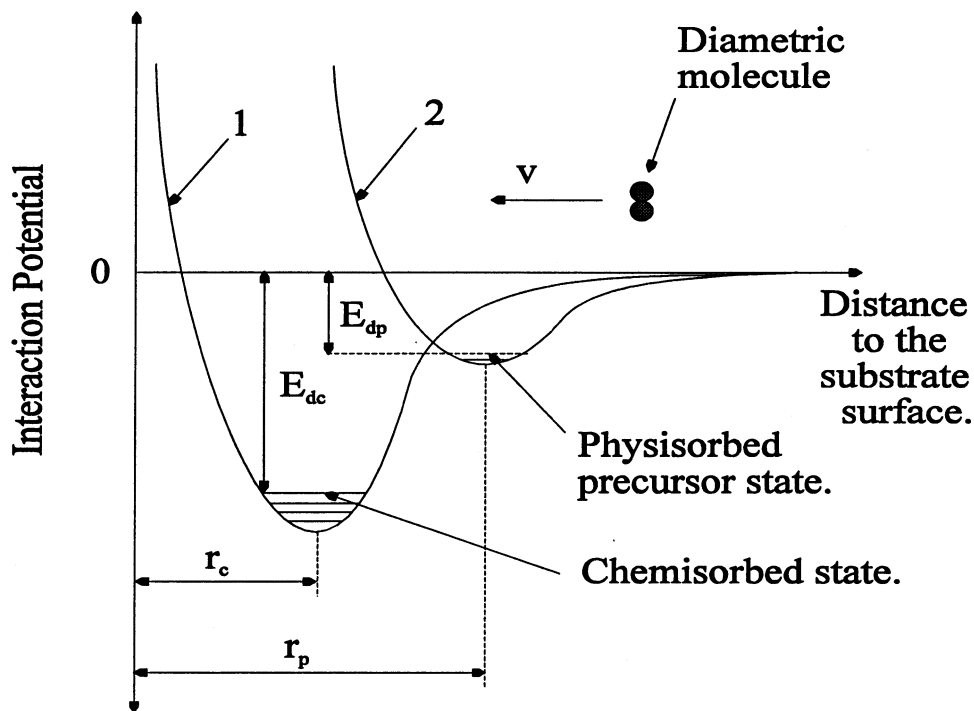


Fig. 1.6: Surface interaction potential for a physisorbed and chemisorbed states [1.23].

It is obvious from the discussion above that not all the atoms which reach the growing surface incorporate (i.e. stick). The probability that an atom incident on the growing crystal surface will remain there is given by the sticking coefficient, defined by:

$$s = \frac{\# \text{ of atoms adhering to the surface}}{\# \text{ of atoms arriving at the surface}} \quad (1.9)$$

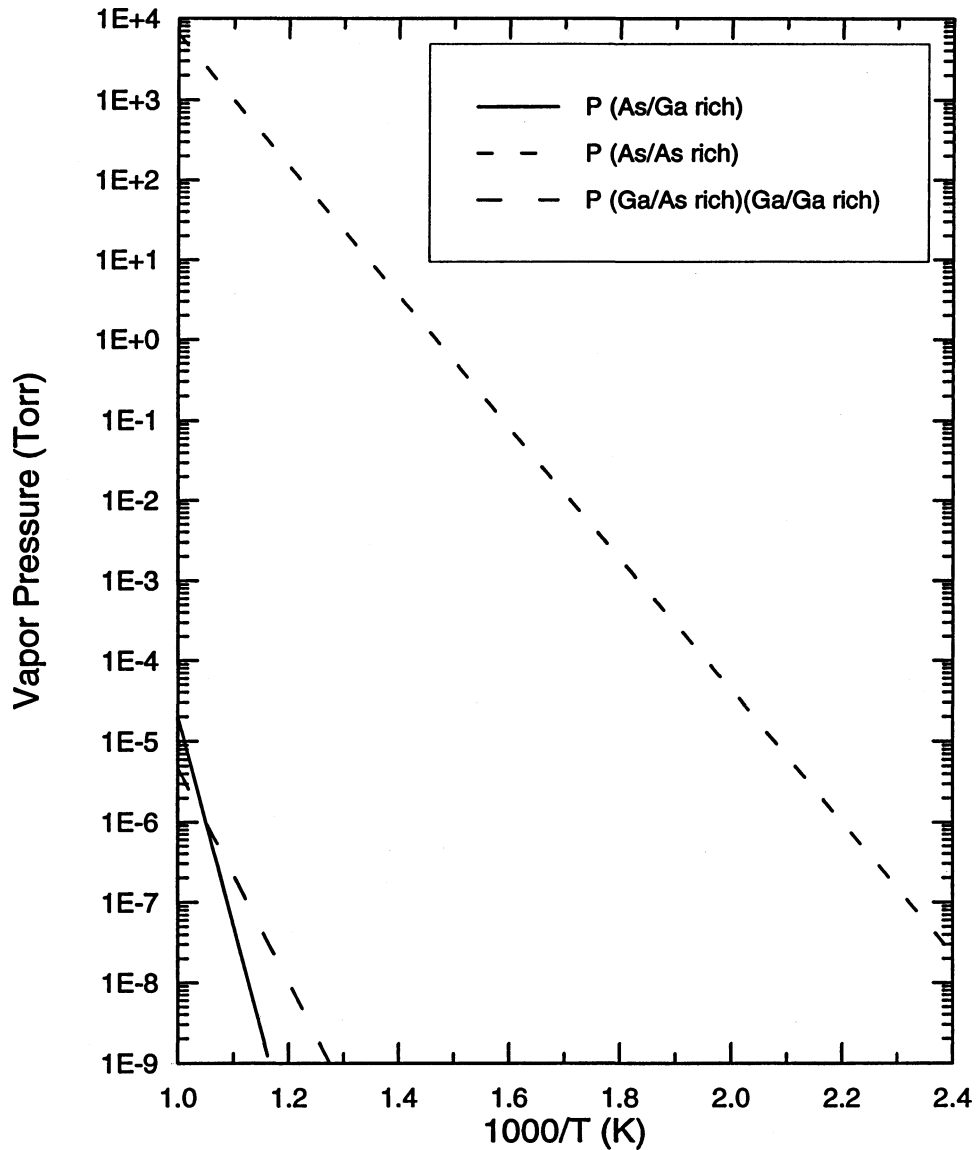


Fig. 1.7: Plot of the vapor pressures of As over As rich GaAs ($P_{As/As\ rich}$), As over Ga rich GaAs ($P_{As/Ga\ rich}$), Ga over As rich GaAs ($P_{Ga/As\ rich}$), and Ga over Ga rich GaAs ($P_{Ga/Ga\ rich}$) [1.24].

A sticking coefficient equal to unity indicates that all the atoms incident on the surface will remain there. The value of the sticking coefficient will be determined by the ratios of the beam equivalent pressure and the vapor pressure of the species on the surface of the growing crystal at the given substrate temperature. Consider Figure 1.7 which shows the vapor pressure of both Ga and As on the different possible crystal surfaces (i.e. Ga and As

rich surfaces). Growing GaAs at 600°C with a Ga beam equivalent pressure of 10^{-6} torr would effectively allow all the Ga to stick on the surface (i.e. a sticking coefficient = 1). This is because a beam equivalent pressure of 10^{-6} Torr is much greater than the vapor pressure of Ga on either an As or Ga rich surface. If the same beam equivalent pressure of 10^{-6} torr is used for As, only the As impinging on a Ga rich surface will stick. Any As impinging on an As rich surface would reevaporate due to the high 100 Torr vapor pressure.

The above argument implies that if GaAs growth occurs in an As rich environment (i.e. with an arsenic equivalent partial pressure larger than the vapour pressure), the ratio of the Ga partial pressure to its vapour pressure will determine the growth rate. Excess arsenic will not be incorporated on the surface because of the high vapour pressure of As on an arsenic rich surface. This permits the growth of high quality material without requiring a high accuracy of beam fluxes.

1.3.3 McMaster Gas Source Molecular Beam Epitaxy System

Figure 1.8 illustrates a schematic diagram of the McMaster GSMBE system. Most growths performed with this system are done using a substrate crystal which is mounted indium free on a molybdenum sample holder. The sample is placed in a load-lock, pumped down and transferred to a trolley line. The sample is then transferred to a pre-deposition chamber (3) where it is heated to 350-400 °C. This pre-heat is used to remove surface moisture before being transferred to the growth chamber. Once in the growth chamber, the sample is heated to the growth temperature in a group V overpressure.

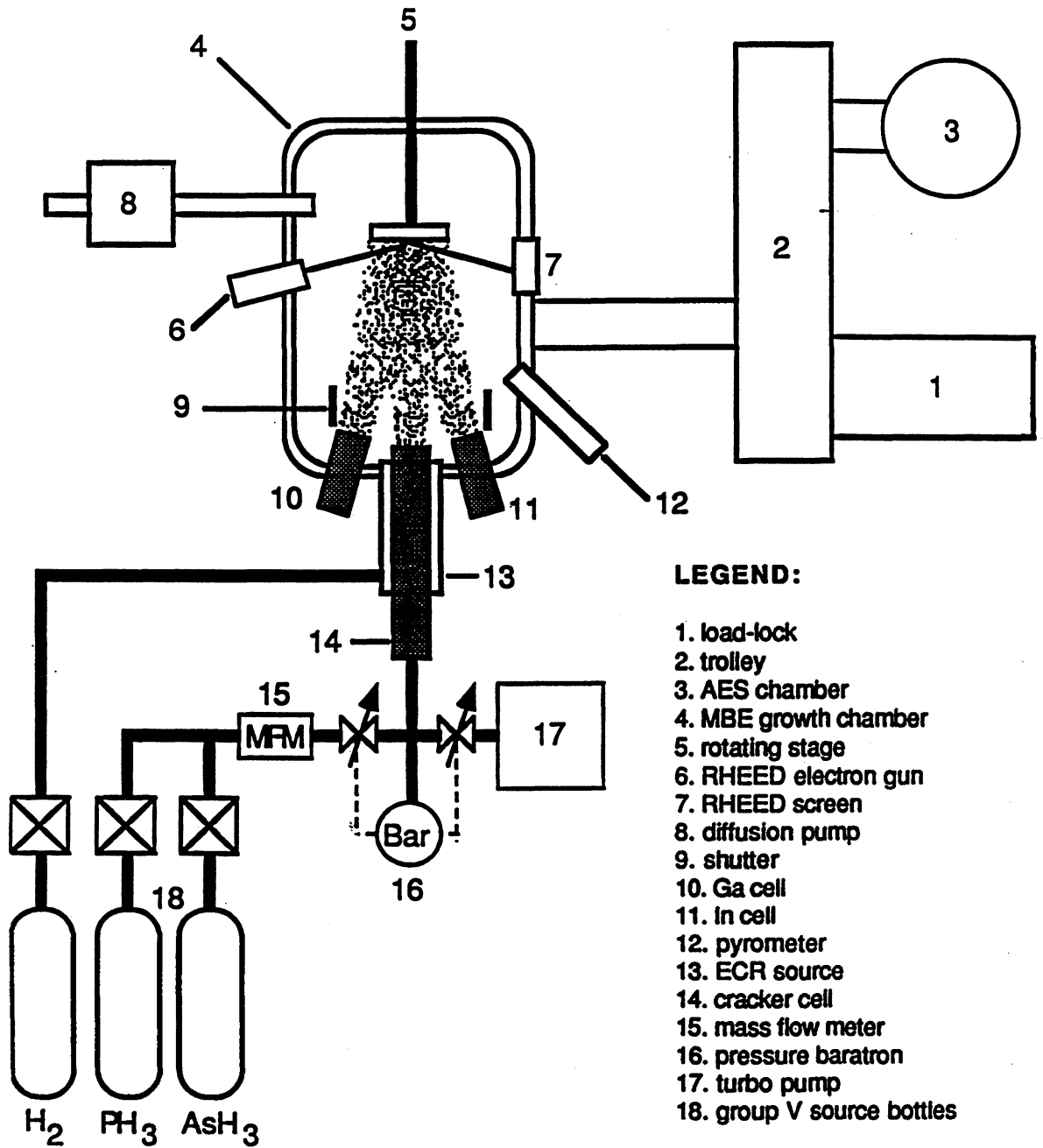


Fig. 1.8: Schematic of the McMaster GS-MBE [1.25]

It is then exposed to a electron cyclotron resonant (ECR) hydrogen plasma. This plasma treatment is used to clean the InP and GaAs substrates, prior to growth, by removing native oxides. The effect of such treatments on the substrate surface and on the quality of material grown has been studied in detail by Robinson et al. [1.26]. After a two minute exposure to the plasma the samples are ready for growth. The typical background pressure for the system prior to growth is 10^{-10} Torr.

2.0 CHARACTERIZATION TECHNIQUES

2.1 Introduction

This section provides a description of characterization techniques employed in this thesis. The first section presents the theory of photoluminescence. This technique was used to optimize the as-grown MBE material. The subsequent section will discuss the characterization of fabricated lasers and the criteria used to judge performance of these devices.

2.2 Photoluminescence

There are numerous techniques used for semiconductor materials characterization which employ electromagnetic radiation as the experimental probe. Table 2.1 contains a list of the semiconductor properties which can be examined using three common optical characterization methods. Of all the semiconductor characterization techniques available photoluminescence spectroscopy is the most widely used for the optimization of crystal growth parameters.

Photoluminescence (PL) is sensitive to many important semiconductor properties: band gap energy, stress, and interface quality in heterostructures. PL is also useful in detecting impurities or dopants and crystal defects. Although all these properties can be measured using other optical characterization techniques, PL is one of the simplest to perform and the required information, in most cases, can be obtained from a single measurement.

Semiconductor Property	Optical Method		
	PL	Raman	IR
Band Structure			
Gap	x		x
Effective mass			x
Offset	x		
Free Carrier			
Concentration		x	x
Mobility		x	x
Scattering Time		x	x
Resistivity		x	x
Lattice			
Alloy composition	x	x	x
Orientation		x	
Crystallinity	x	x	
Stress'	x	x	
Impurity and defect			
Presence and type	x	x	x
Concentration	x	x	x
Microstructure			
Layer thickness			x
Surface behavior	x	x	
Interface behavior	x	x	x
Layer-by-layer behavior			x

Table 2.1: Semiconductor properties which can be characterized by the following optical methods: photoluminescence (PL), Raman spectroscopy (Raman) and infrared absorption spectroscopy (IR) [2.1].

2.2.1 Theory

The recombination of holes in the valence band (with energy E_h) with electrons from the conduction band (with energy E_e), results in the emission of a photon of energy:

$$h\nu = E_e - E_h. \quad (2.1)$$

Therefore, the intensity of the emitted light with energy $h\nu$ should be proportional to the product of the density of electrons in the conduction band at energy E_e (given by $n(E_e)$) and holes in the valence band at energy E_h (given by $p(E_h)$). Under equilibrium conditions the electron and hole densities are given by [2.2]:

$$n(E_c) = \rho_c(E_c)f(E_c), \quad (2.2)$$

$$p(E_h) = \rho_v(E_h)[1 - f(E_h)]. \quad (2.3)$$

Where ρ_c and ρ_v are the densities of state in the conduction and valence band given by:

$$\rho_c(E_c) = \left(\frac{1}{2\pi^2} \right) \left(\frac{2m_c^*}{\hbar} \right)^{\frac{3}{2}} (E_c - E_c)^{\frac{1}{2}}, \quad (2.4)$$

$$\rho_v(E_h) = \left(\frac{1}{2\pi^2} \right) \left(\frac{2m_h^*}{\hbar} \right)^{\frac{3}{2}} (E_v - E_h)^{\frac{1}{2}}, \quad (2.5)$$

and $f(E)$ is the Fermi function which gives the ratio of filled states to the total allowed states at a given energy:

$$f(E_{e,h}) = \frac{1}{1 + e^{\frac{(E_{e,h} - E_f)}{kT}}}, \quad (2.6)$$

where E_f is the Fermi energy level. The Fermi function gives the probability of a state at a given energy in the conduction band being occupied by an electron and one minus the Fermi function gives the probability of a hole occupying a given energy level in the valence band at equilibrium. Therefore, as the Fermi energy increases the number of electrons in the conduction band increase and the number of holes in the valence band decrease.

Photoluminescence measurements are performed by illuminating the semiconductor with monochromatic light of energy greater than the bandgap energy to produce electron-hole pairs. This increases the number of holes in the valence band and electrons in the conduction band simultaneously. This non-equilibrium situation cannot

be represented with the use of a single fermi energy. Therefore, a quasi-fermi energy model [2.3] is used (see Figure 2.1). In this model, the single equilibrium fermi energy is replaced by one for each band, a quasi-fermi energy for electrons, E_{fn} , and for holes, E_{fp} . Therefore, using Eq.'s 2.2 and 2.3, we may write the carrier concentrations under non-equilibrium conditions as:

$$n(E_c) = \rho_c(E_c) f_n(E_c), \quad (2.7)$$

$$p(E_v) = \rho_v(E_v) [1 - f_p(E_v)], \quad (2.8)$$

where $f_{n,p}(E)$ is the quasi-fermi function for holes and electrons given by:

$$f_{n,p}(E_{e,h}) = \frac{1}{1 + e^{\frac{(E_{e,h} - E_{f_{n,p}})}{kT}}}. \quad (2.9)$$

The energy separation of E_{fn} and E_{fp} (and hence the intensity of the emitted PL light) will depend on the intensity of the illuminating light and the efficiency of electron-hole production.

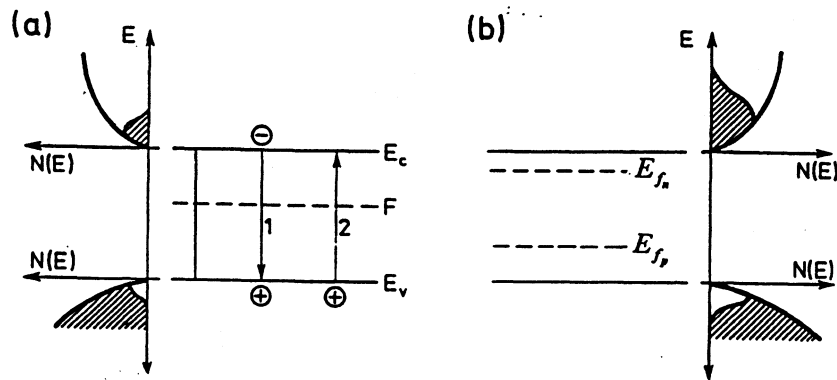


Fig. 2.1: Fermi level for a) semiconductor in equilibrium state and b) semiconductor not in equilibrium state [2.3].

When electrons in the conduction band recombine with holes in the valence band, transitions which conserve momentum will dominate, since they are more probable. This is the k -selection rule [2.4]. Therefore, the conduction and valence band density of states is replaced by the Optical Joint Density of States function. This function only considers transitions between the conduction and valence bands for which the momentum will be conserved:

$$\rho(h\nu) = \frac{(2m_r)^{\frac{3}{2}}}{\pi\hbar^2} (h\nu - E_g)^{\frac{1}{2}}, \quad (2.10)$$

where m_r is the electron-hole reduced mass.

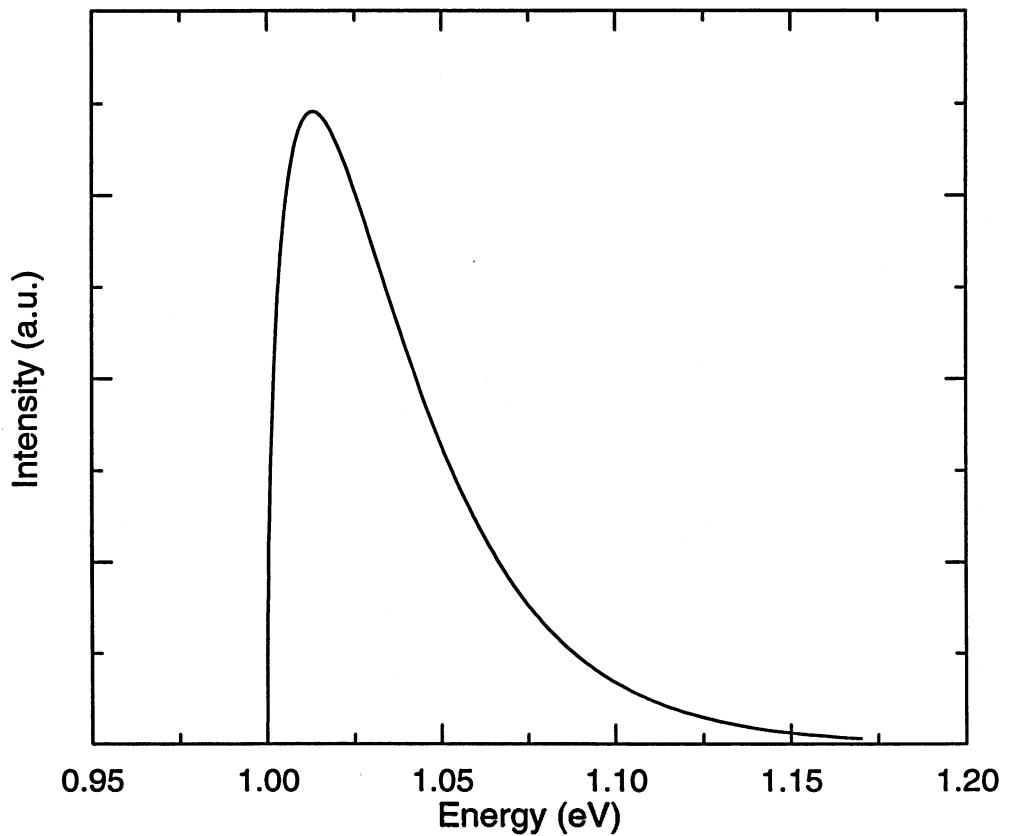


Fig. 2.2 : Graph of intensity vs emitted photon energy for an arbitrary semiconductor with 1 eV bandgap energy.

From Eq.'s 2.7-10 we can obtain the Van Roosbroeck-Shockley expression for spectral line shape [2.5]:

$$I(h\nu) = C(h\nu - E_g)^{\frac{1}{2}} e^{\left(-\frac{h\nu - E_g}{kT}\right)}, \quad (2.11)$$

where C is a constant and E_g is the band gap energy. Figure 2.2 shows a graph of Eq. 2.11. The low energy edge of Figure 2.2 corresponds to the energy gap and the slope of the high energy portion is related to the carrier temperature.

2.2.2 Transition Characteristics

The theory presented above adequately describes the general properties of conduction to valence band transitions (also called free carrier recombination). Most PL spectra contain much more structure than Figure 2.2, due to transitions not accounted for in our simple model. These include exciton recombination, band to impurity or donor to acceptor transitions, each of which has a particular signature.

When a semiconductor is cooled to low temperature and illuminated, the generated electrons and holes bind together due to mutual Coulomb attraction. These atom like complexes are called excitons. Just like an atom, excitons can have several binding energy states (E_{x_n}) which are given by [2.6]:

$$E_{x_n} = \frac{m_r^* q^4}{2h^2 \epsilon^2} \frac{1}{n^2} \quad \text{for } n = 1, 2, 3, \dots, \quad (2.12)$$

where m_r^* is the reduced mass of the electron-hole system. When free excitons recombine they emit light at an energy:

$$h\nu = E_g - E_{x_n} \quad , \quad (2.13)$$

In most cases only the $n = 1$ peak is observed since the emission intensity of the higher order exciton states decreases as $1/n^3$ [2.7]. The width of the free exciton peak represents the kinetic energy distribution of the electron-hole pair.

In the case when excitons are localized in the vicinity of a donor, acceptor, or neutral impurity they form bound excitons [2.6]. Since they lack the kinetic energy of free excitons, bound excitons recombine to form a peak which is much narrower and is centered about:

$$h\nu = E_g - E_{x_n} - E_b \quad , \quad (2.14)$$

where E_b is the energy associated with the bond between the exciton and the impurity. The magnitude of E_b is dependent on the type of impurity and therefore provides a signature for the impurity. The linewidth can also be used to give an indication of material quality since these sharp photoluminescence peaks are quite sensitive to local strains in the material[2.1].

Another possible radiative process involves transitions to and from localized impurities. Free-to-bound emission results from transitions between free electrons in the conduction band and acceptors. Although radiative emission is also possible between donors and holes in the valence band, most donors in III-V semiconductors are very

shallow so that emission is rarely observed at temperatures above 10 K [2.6]. The photon energy of free to bound emission is given by:

$$h\nu = E_g - E_a, \quad (2.15)$$

where E_a is the ionization energy of the donor or acceptor. The line width of this emission peak is mainly governed by the kinetic energy distribution of the electrons (i.e. the electron temperature) involved in the recombination.

Transitions between donor and acceptor sites are also possible. These transitions, which are most apparent in highly compensated materials, have an emission peak energy which is dependent on the average physical distance between donors and acceptors. For any given donor-acceptor pair separated by a distance r the emitted photon energy is given by [2.6]:

$$h\nu = E_g - (E_A + E_D) + \frac{e^2}{\epsilon r}, \quad (2.16)$$

where E_A and E_D are the acceptor and donor energy levels.

All the transitions described above are only observed in high purity binary semiconductors. In general only two lines are observed during the low temperature photoluminescence of ternary and quaternary semiconductors [2.8]. The strongest line is due to excitonic transitions and the other results from the merging of bound to free and donor to acceptor transitions. In addition, PL peaks from ternary and quaternary semiconductors tend to be broader. This is due to statistical fluctuations in the materials composition which causes local fluctuations in the band gap. This will broaden the spectra from all electron-hole emission processes [2.9].

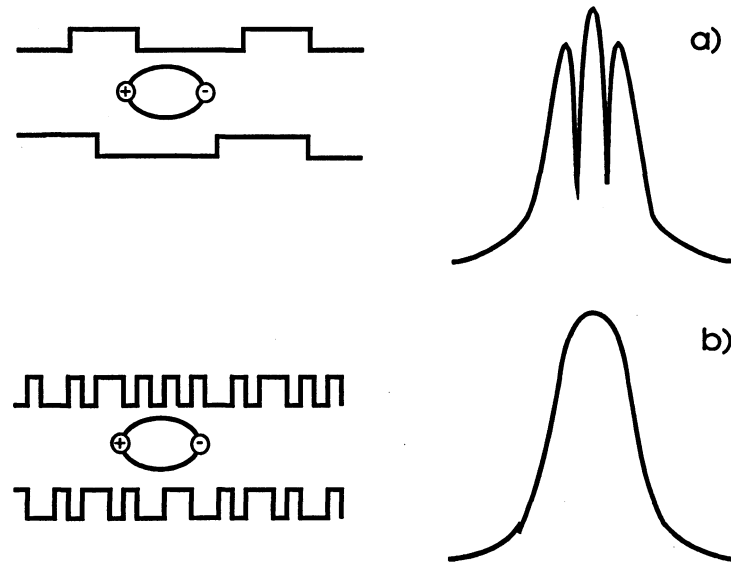


Fig. 2.3: Shape of PL emission for QW with smooth (a) and rough (b) interface [2.10].

In this work, PL is used to optimize the growth conditions for strained QW structures. The low temperature PL emission peaks for such structures are typically excitonic in nature and are centered about a wavelength given by Eq. 1.8. The full width at half maximum (FWHM) of PL emission from such structures is highly dependent on the quality of the interface between the materials which form the well [2.10]. In the case of binary QWs with smooth interfaces, the PL spectrum exhibits multiple peaks which correspond to the three different energy regimes in the well. These different energy regimes arise from variations in local well widths (\pm one monolayer) which are larger than the exciton radius (see Figure 2.3a). For wells with rougher interfaces a single peak is observed (see Figure 2.3b) and its width gives an indication of the degree of interface roughness. However, in strained ternary and quaternary QWs only a single peak is observed. This is due to the broadening effects caused by both strain, compositional fluctuations. Under these conditions, the peak FWHM can be used as a qualitative

comparison of interface quality between wells of equal width, strain, and alloy composition.

2.2.3 Experimental Setup

The experimental setup for PL spectroscopy shown in Figure 2.4. Optical excitation of the sample is achieved by a laser whose photon energy is larger than the band gap of the semiconductor being probed. An Ar ion laser is well suited due to its high photon energy, 2.54 eV, which exceeds the band gap of most III-V semiconductors. Light from the laser is filtered through F2 to remove other lasing and non-lasing lines which are in the spectral region of interest. The laser light is then directed onto the sample surface by an adjustable mirror. The sample is usually placed in a cryostat which is used to lower the sample temperature close to that of liquid helium. This is necessary to reduce the thermal broadening (equal to kT) which would hide less intense transitions because of the thermal tailing from neighboring transitions in the PL spectrum.

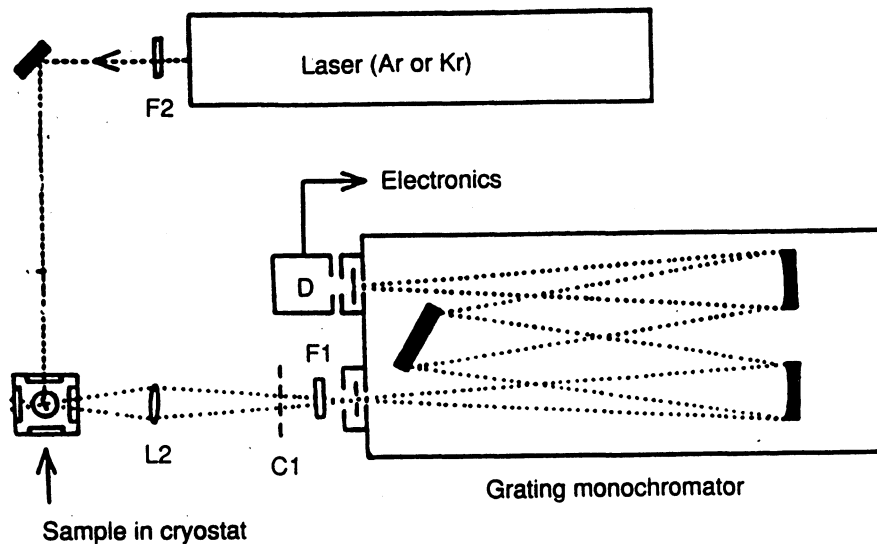


Fig. 2.4: PL spectroscopy setup [2.1]

The PL light, which is emitted from the surface of the sample, is focused by a lens (L). It then passes through a chopper (C1). The chopper modulates the PL emission so a lock-in amplifier can be used to narrow the measured bandwidth, improving the signal to noise ratio. Following the chopper, the light passes through a filter (F1), to remove the reflected laser pump light, before entering the monochromator. The PL light entering the monochromator is separated into different wavelength components and the chosen wavelength is directed to the detector (D). The detector can be a photomultiplier tube or a photodiode, the choice depending on the spectral region of interest.

2.3 Laser Characterization

All the devices in this thesis were compared using the fundamental laser operating characteristics which can be extracted from Power vs Applied Current (P-I) measurements. Internal quantum efficiency (η_i), total optical loss per unit length (α) and threshold current density (J_{th}) are the three key parameters.

The threshold current density is defined by Agrawal [2.11] as the current density required to achieve threshold gain (g_{th}) (i.e. the point where the gain in the laser cavity is equal to the losses in the cavity). The threshold current density is related to the threshold current I_{th} by the relationship:

$$J_{th} = \frac{I_{th}}{WL}, \quad (2.17)$$

where W is the width of the pumped area and L is the cavity length. The threshold current I_{th} of a laser can be extracted directly from its P-I plot. It is the point at which the laser is said to turn on (see Figure 2.5).

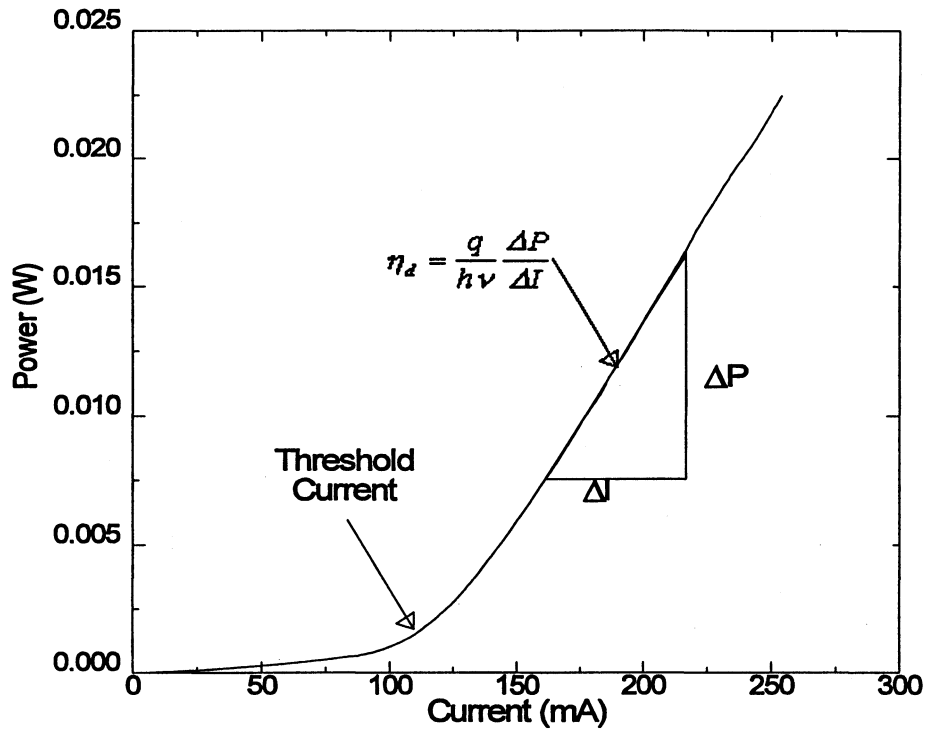


Fig. 2.5: P-I plot for 50x300 mm broad area laser showing the threshold current and determination of external quantum efficiency.

Internal quantum efficiency is defined as the ratio between the radiative electron-hole (r_r) recombination and the total recombination rate (r) [2.4]:

$$\eta_i = \frac{r_r}{r} = \frac{r_r}{r_r + r_m}, \quad (2.18)$$

where r_m is the nonradiative recombination rate. Nonradiative recombination takes place via defect centers in the bandgap. The higher the concentration of these centers, the higher the nonradiative recombination rate and hence the lower the internal quantum efficiency. The internal quantum efficiency can be obtained from the relation [2.11]:

$$\eta_d^{-1} = \eta_i^{-1} \left[1 + \frac{\alpha_i L}{\ln(1/R)} \right] \quad (2.19)$$

where R is the cavity reflectivity, L is the cavity length and η_d is the external quantum efficiency. The external quantum efficiency is obtained from the slope of the P-I plot just above the threshold point and is given by the relation:

$$\eta_d = \frac{q}{h\nu} \frac{\Delta P}{\Delta I} \quad (2.20)$$

Using equations 2.19 and 2.20, one can obtain the internal quantum efficiency from the y-intercept of a plot of inverse external quantum efficiency vs. cavity length.

The total optical loss, α (also called the intrinsic loss) can be obtain from the slope of the inverse external quantum efficiency vs. cavity length plot. The total optical loss is given by [2.11]:

$$\alpha = \alpha_{sc} + \Gamma\alpha_{in} + (1 - \Gamma)\alpha_{ex} \quad (2.21)$$

Here α_{sc} is the scattering loss out of the waveguide region. The stronger the waveguide the smaller α_{sc} . The terms α_{in} and α_{ex} are due to loss mechanisms in the active region and cladding respectively. The losses are dominated by free carrier absorption at high current injection levels and by absorption centers in the barrier and cladding regions at low carrier injection conditions.

Using these parameters derived from the experimental data allows the quantitative comparison of different lasers.

3.0 LASER FABRICATION

3.1 Introduction

The fabrication process is the most important part of the work presented in this thesis. During laser fabrication small errors, such as forgetting a solvent clean or sloppy clean room protocol, can make the difference between functioning and non working devices. Reproducibility is also an important aspect of laser fabrication especially when the characteristics of lasers from different processing batches are to be compared. For this reason it is necessary to construct and follow a well planned procedure which includes the largest conceivable amount of detail.

In this thesis both broad area and ridge waveguide lasers were fabricated. The following sections will give details of the important aspects of laser fabrication (such as sample cleaning and photolithography) as well as outline the fabrication of both these laser types.

3.2 Sample Cleaning

Cleaning refers to the removal of undesirable materials from the surface of a sample before subsequent processing steps. These unwanted materials can be organic (i.e. oils, greases, and photoresist), or inorganic contaminants (i.e. dust particles, metal particles, native oxides and moisture). Incomplete or improper removal of any organic or inorganic contaminates results in poor metal adhesion, interferes with photolithographic processes and causes unwanted masking during wet or dry etching.

Since no single cleaning step can remove all unwanted contaminants from a sample surface, three cleaning steps were used for the laser fabrication work completed in this thesis. Each of these procedures addresses the removal of a particular type of contaminant. The first procedure is used to remove particle contamination. For this cleaning step the sample is placed on the resist spinner and spun at 4000 rpm while the surface is blown clean with a nitrogen gun. It is important that this cleaning step be done before any solvent clean, since a solvent will remove any oils or greases which surround the particles leaving them dry and firmly adhered to the sample surface.

The next cleaning step involves the removal of organic material from the surface. This is usually accomplished using a solvent clean. The solvents used in this thesis are listed in Table 3.1. Since the samples are cleaned by immersion, the debris removed from the samples accumulates in the solvent. For this reason two batches of each solvent is used.

Solvent	Batch	Total Cleaning Time (mins)	Cleaning Temp. (°C)
Acetone	1)	10	50
Trichloroethylene	1)	5	60
Methanol	1)	5	60

Table 3.1: Organic solvents used for sample cleaning.

During a solvent clean the samples are first immersed in acetone to remove Photoresist from previous processing steps. If no resist has been applied to the surface this step may

be omitted. The samples are then immersed in trichloroethylene to remove any organic material which remains on the surface of the sample. Although acetone can also be used to remove organic material trichloroethylene is much more aggressive, leaving a cleaner surface. The final step in the solvent clean is an immersion in methanol. This step is used to remove any trichloroethylene or acetone film which may still be present on the surface. Finally the samples are rinsed in DI water and blown dry with nitrogen.

The third and final cleaning step involves the removal of surface native oxides. This cleaning step, which is only used prior to metal deposition, improves metal adhesion to the semiconductor surface and the quality of ohmic contacts. For this cleaning step the samples are immersed in 20:1 of DI water and HCl for about 30 seconds. The samples are then rinsed in DI water for 30 seconds and blown dry with nitrogen. It is important this cleaning step be done just before the samples are loaded into the metalization chamber, since ordinary exposure to air can slowly reoxidize the sample surfaces. The diluted HCl etch is only effective in removing GaAs native oxides. If a contact is being placed on a different semiconductor surface an alternative etchant should be used (example: diluted HF will remove InP native oxides).

3.3 Photolithography

The devices processed in this thesis were all fabricated using standard photolithographic techniques. This involves applying resist to the sample surface and selectively exposing the resist using a photomask and UV source. The resist films are then subjected to a development process that selectively removes all the exposed positive

resist, or unexposed negative resist. The pattern is then transferred to the sample surface by using the photoresist as a mask to etch the sample surface or in a liftoff to selectively deposit metal on the sample surface.

In order to develop a reproducible and reliable photoresist masking process the following parameters can be varied: resist spin speed and time, softbake temperature, exposure dose and development time. The resist spin speed and time defines the resist thickness and uniformity. For the Shipley S1808 resist, used in the thesis, the thickness when spun at 4000 rpm is approximately 0.8 μm . Spinning for 30 seconds is enough to ensure good uniformity. Any changes in the resist thickness, due to changing the resist spin speed, would require changes in the subsequent process steps. After the resist has been spun on the sample it is soft baked at 110 $^{\circ}\text{C}$. This step drives off most of the solvent contained in the film, improves adhesion to the surface and makes the surface less tacky (this prevents the mask from sticking to the surface during the exposure process).

After the resist has been spun and soft baked, the sample is then ready to be exposed with the appropriate mask. All the exposures were performed using a Karl Suss MJB3 mask aliner. The key parameter in an exposure is called the Exposure Dose (D) and is given by:

$$D = I \times t \tag{3.1}$$

where I is the intensity of the exposing light source at 365 nm, the main line of the light source to which the resist is sensitive, and t is the duration of the exposure. For positive resist, the exposure dose increases the dissolution rate of the exposed resist in the developer solution. Therefore, the dose must be large enough that the dissolution contrast

is high (i.e. the ratio of the exposed and unexposed resist dissolution rate is large). However, if the exposure dose for a given development time is too high the resolution of the pattern will be compromised. Hence the way to proceed is to set a fixed development time and adjust the exposure dose so that good resolution is obtained (for the S1808 resist a dose of 28 mJ/cm^2 for a development time of 30s gives good resolution). Following 30 seconds in the developer, the resist must be "hard baked" at $110 \text{ }^\circ\text{C}$. This step drives off the remainder of the solvent and hardens the resist pattern making it more resistant to any chemicals which will be used in transferring the resist pattern onto the sample.

The process described above results in a resist profile with vertical walls as seen in Figure 3.1a. This profile is ideal when the pattern is transferred to the sample by chemical etching. If the pattern is to be used for the selective deposition of metal via a liftoff process, the profile in Figure 3.1 b is preferred. The "lip" on the top of the profile prevents metal from depositing along the resist side walls. This ensures that no metal on the resist is connected to the metal on the sample surface. This allows a proper liftoff process to occur.

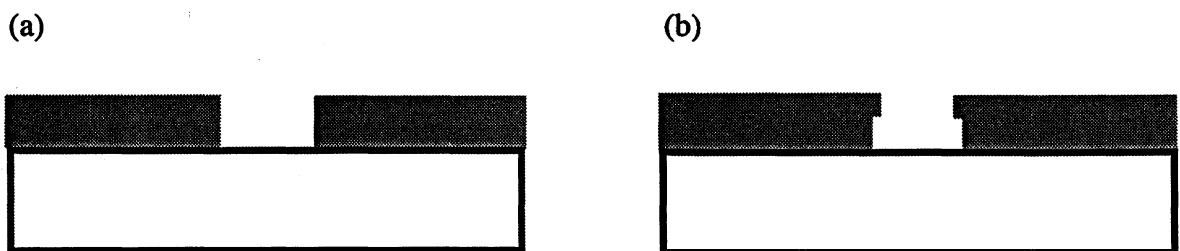


Figure 3.1: Resist profiles for (a) etch mask process and (b) liftoff mask process.

In order to create the lip in Figure 3.1b it is necessary to harden the surface of the resist (about a 1000 Å deep) so that its dissolution rate in developer is less than that of either the exposed or the unexposed resist. This can be achieved in several ways, the most common of which is immersion in toluene or chlorobenzene. This removes the solvent from the surface of the resist without dissolving any of the resin thus hardening the surface. With S1808 resist the samples are soaked in toluene for seven minutes just prior to development. Since the toluene soak also hardens the exposed areas of the resist the development time is extended to 2.5 minutes.

3.4 Laser Processing

In this thesis both broad area and ridge waveguide lasers were fabricated. The fabrication steps for these lasers are similar. The fabrication of ridge waveguide lasers requires a few extra steps which define the ridge. Hence the fundamental steps for ridge waveguide laser fabrication will be described. The processing sequence is as follows:

1. Following a full wafer clean (as described in section 3.2), photoresist is used to pattern the samples with a ridge etch mask. The orientation of the ridges is such that they were perpendicular to the major flat (i.e. along the (0, 1, 1) direction).
2. The ridge structures are formed by wet chemical etching. First the GaAs p-cap is etched using a 1:8:160 H₂SO₄:H₂O₂:H₂O mixture, then a 1:1 HCl:H₃PO₄ mixture is used to etch the InGaP down to the GaAs etch stop (see Figure 3.2 (b)).

3. The resist mask is then removed from the sample with a solvent clean and the sample is coated with a 1000 Å thick silicon dioxide layer.

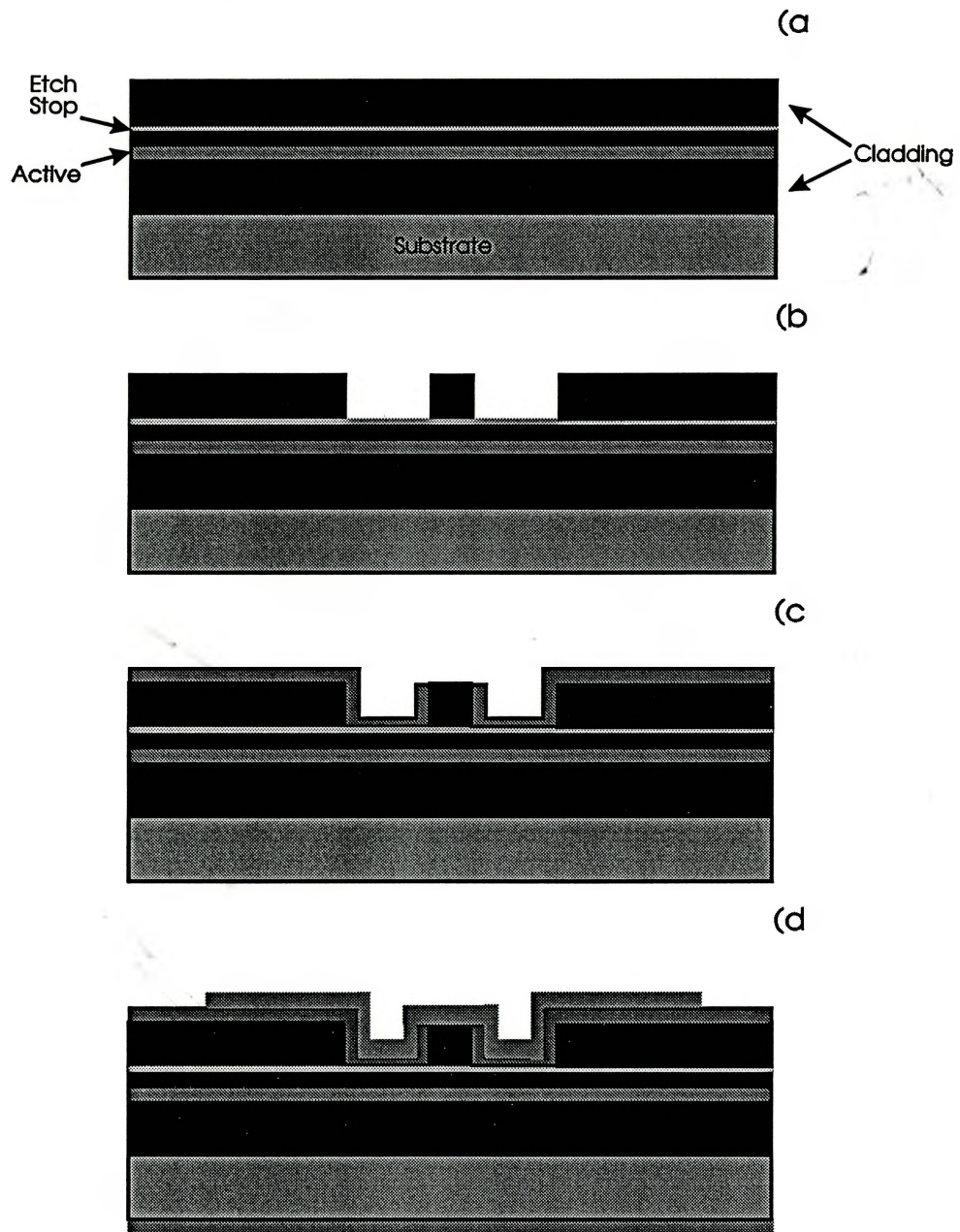


Fig. 3.2 : Ridge waveguide laser process flow: (a) Structure outline, (b) Etched ridge, (c) Silicon dioxide passivated ridge with open contact area on ridge, and (d) Finished RWG laser with p- and n-type metal contacts.

4. The samples are then patterned with an etch mask which exposes the oxide on the surface of the ridge structure. This oxide is etched off in a buffered oxide etch leaving the GaAs p-cap exposed. The mask is then removed and the sample is cleaned (see Figure 3.2 (c)).
5. Next the samples are patterned using a liftoff process leaving the ridge and surrounding area exposed. The native oxide of the exposed semiconductor on top of the ridge is first removed in a 1:20 HCl:DI etch and a Ti/Pt/Au p-contact layer is deposited over the surface. The samples are then soaked in acetone to liftoff the unwanted metalization.
6. The sample is then thinned to about 150 μm by lapping and polishing the substrate side.
7. Finally the native oxide is removed from the substrate side in a 1:20 HCL:DI etch and the n-contact is formed by depositing a Ni/Ge/Au contact and annealing the sample at 400 $^{\circ}\text{C}$ for 30 seconds (see Figure 3.2 d).

With the wafer fabrication complete, the samples are ready to be cleaved into laser bar with cavity lengths ranging from 500 to 1500 μm . At this point the lasers may undergo preliminary tests or may be cleaved into individual die and bounded to a copper heatsink. For the fabrication of broad area lasers steps 1 and 2 are omitted.

4.0 OPTIMIZATION RESULTS

4.1 Introduction

In this section, the work undertaken to produce CW (constant wave or DC) 980 nm ridge waveguide lasers is presented. This development was deemed necessary based on the poor results of the first 980 nm lasers grown and fabricated at McMaster University. Figure 4.1 shows a typical power versus current (P-I) plot for the first set of devices clearly demonstrating the poor quality. Based on these results, a three part study was initiated. Part one involved the growth optimization of the InGaAs QW, which makes up the active region of these lasers, using photoluminescence to find the best growth conditions for these structures. In order to draw correlation between QW material properties and laser characteristics, the second part of this study involved the growth,

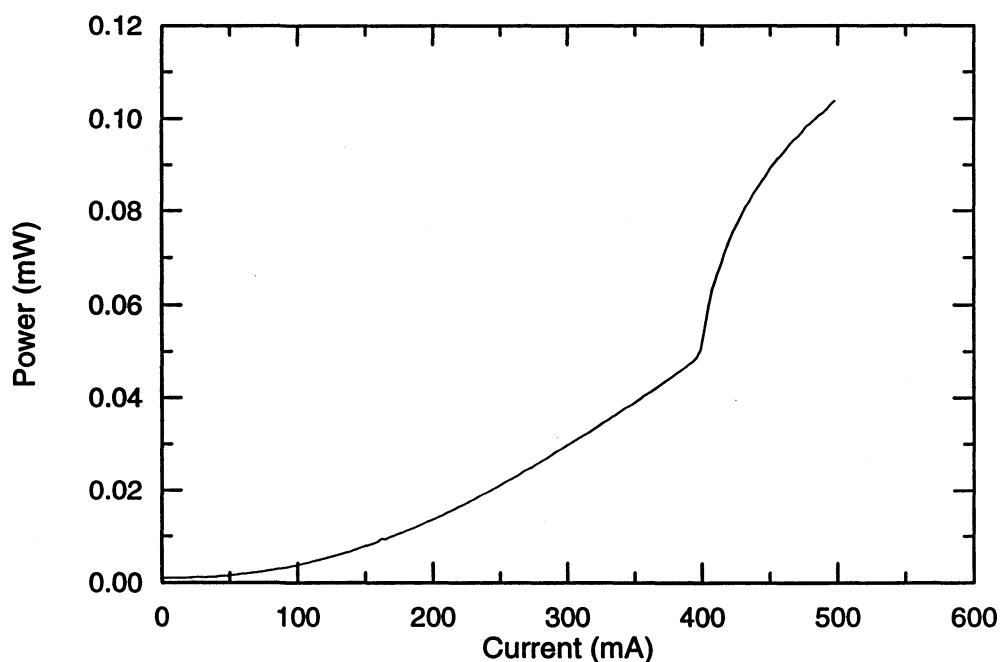


Fig. 4.1: Pulsed P-I plot of 30 μ m strip broad area laser (0.2 μ s pulse width and 1 % duty cycle).

fabrication and characterization of broad area lasers. Finally the information gathered from these studies was used to define the growth parameters for a ridge waveguide laser structure.

4.2 QW Optimization

The active area of the 980 nm laser, to be fabricated, consists of a 10 nm QW layer of $\text{In}_{0.20}\text{Ga}_{0.80}\text{As}$ between two GaAs barrier layers. The role of the QW is to capture electrons and holes so they may recombine to produce photons. The quality of the materials which constitute the well and the interfaces between the various materials can greatly affect the efficiency with which electron-hole pairs are converted into photons. In order to produce a QW with good material and interface quality, the optimum growth conditions must be found. Growth of QW structures by MBE provides the researcher with a large parameter space of growth conditions which can be varied. Growth temperature, growth rate, group V overpressure and growth interruption time at the various interfaces can all be varied to achieve good material properties. Since the goal of this thesis was to produce CW lasers in a fixed time frame, it was impossible to investigate the whole gamut of possible growth conditions. Hence only a few parameters were investigated over a limited range of possible values.

The first parameter to be investigated was growth temperature (i.e. substrate temperature). The initial set of growths addressed the issue of the difference in optimal growth temperatures for both InGaAs and GaAs (460-520°C [4.1] and 580-680°C [4.2] respectively). For this study three samples were grown (see Figure 4.2 for the layer

GaAs	300 nm	undoped
InGaAs	10 nm	undoped
GaAs	400 nm	undoped
Substrate		

Fig. 4.2: Sample QW structure for growth optimization studies.

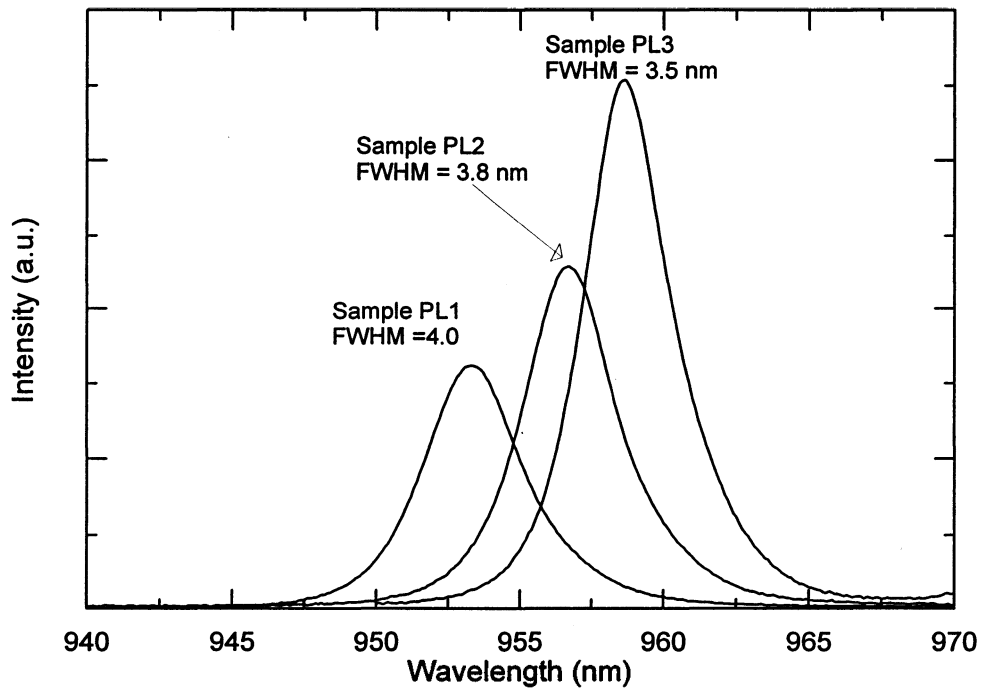


Fig. 4.3: PL spectra at 11 K of QW samples in the growth temperature study.

structure). The growth conditions of the InGaAs layer were the same for all three samples (see Table 4.1). The growth temperature used for the InGaAs layer was obtained from G. Zang [4.3] and is used as a starting point in the optimization of the QW growth parameters. The GaAs layer, on the other hand, was grown with the same group V flow and growth rate (the Ga flux was also adjusted at each interface in order to maintain a

constant growth rate) as the InGaAs layer but its growth temperature was varied from 580 to 515 °C. These samples would indicate whether or not the GaAs barrier layers should be grown at the same temperature as the QW or closer to the optimum growth temperature for GaAs. It should be noted that since the substrate and/or the Ga flux needed to be adjusted for each layer in the growth it was impossible to maintain a constant growth interruption time for all 3 samples in this first study. The PL results from these samples are summarized in Figure 4.3.

Sample #	GaAs Growth Temperature (°C)	InGaAs Growth Temperature (°C)	Growth Rate (μm/hr)	Group V Flow Rate (sccm)
PL1	580	515	1	3.9
PL2	550	515	1	3.9
PL3	515	515	1	3.9

Table 4.1: QW growth parameters for the growth temperature optimization study.

The results of this study show that as the growth temperature of the GaAs barrier layer is increased, from that of the $\text{In}_{0.20}\text{Ga}_{0.80}\text{As}$ layer towards a growth temperature which yields better quality bulk GaAs material (see [4.2]), the optical properties of the QW degrade. This is accompanied by a steady decrease in emission wavelength as the temperature is increased from 515 to 580°C. This is caused by the re-evaporation of Indium from the surface of the $\text{In}_{0.20}\text{Ga}_{0.80}\text{As}$ layer, which occurs while the substrate temperature is being increased from the $\text{In}_{0.20}\text{Ga}_{0.80}\text{As}$ growth temperature to the GaAs growth temperature. This effect reduces the width of the QW and thus decreases the emission wavelength.

The results of the above study demonstrate that the optical properties of the QWs are best when both the barrier and well layers are grown at the same temperature. This

may be due to the long growth interruption times at the interfaces while waiting for substrate temperatures to change. This is known to have a detrimental affect on the optical properties of QWs [2.10]. These results are taken into consideration in the design of the second growth study to investigate the effect of the group V flow rate (i.e. As₂ overpressure) on the optical properties of the InGaAs QW structures. For this study two sets of identical structures were grown, both sets consisting of four growths: the first at 515°C and the second at 485°C. The growth parameters are summarized in Table 4.2. The GaAs barrier region for all the samples was grown at 0.8 μm/hr. When the InGaAs layer was grown the In shutter was opened, increasing the growth rate to 1 μm/hr and yielding the 20 % In composition required. The In shutter was then closed again for the next GaAs barrier. At each interface both the In and Ga shutters were closed thus interrupting the growth for ten seconds. By performing the growths in this fashion and growing the layers at the same temperature, the growth interruption time at the InGaAs/GaAs interface can be set, since waiting for the cell and substrate temperatures to change is not necessary. It should be noted that some samples were grown with flow rates below 2.5 sccm, but these samples exhibited poor crystalline properties due to insufficient As.

Sample #	Growth Temperature (°C)	Flow Rate (sccm)	Growth Interruption (sec)
PL4	515	4.3	10
PL5	515	3.6	10
PL6	515	2.8	10
PL7	515	2.5	10
PL8	485	4.3	10
PL9	485	3.6	10
PL10	485	2.8	10
PL11	485	2.5	10

Table 4.2: QW growth parameters for Group V flow rate study.

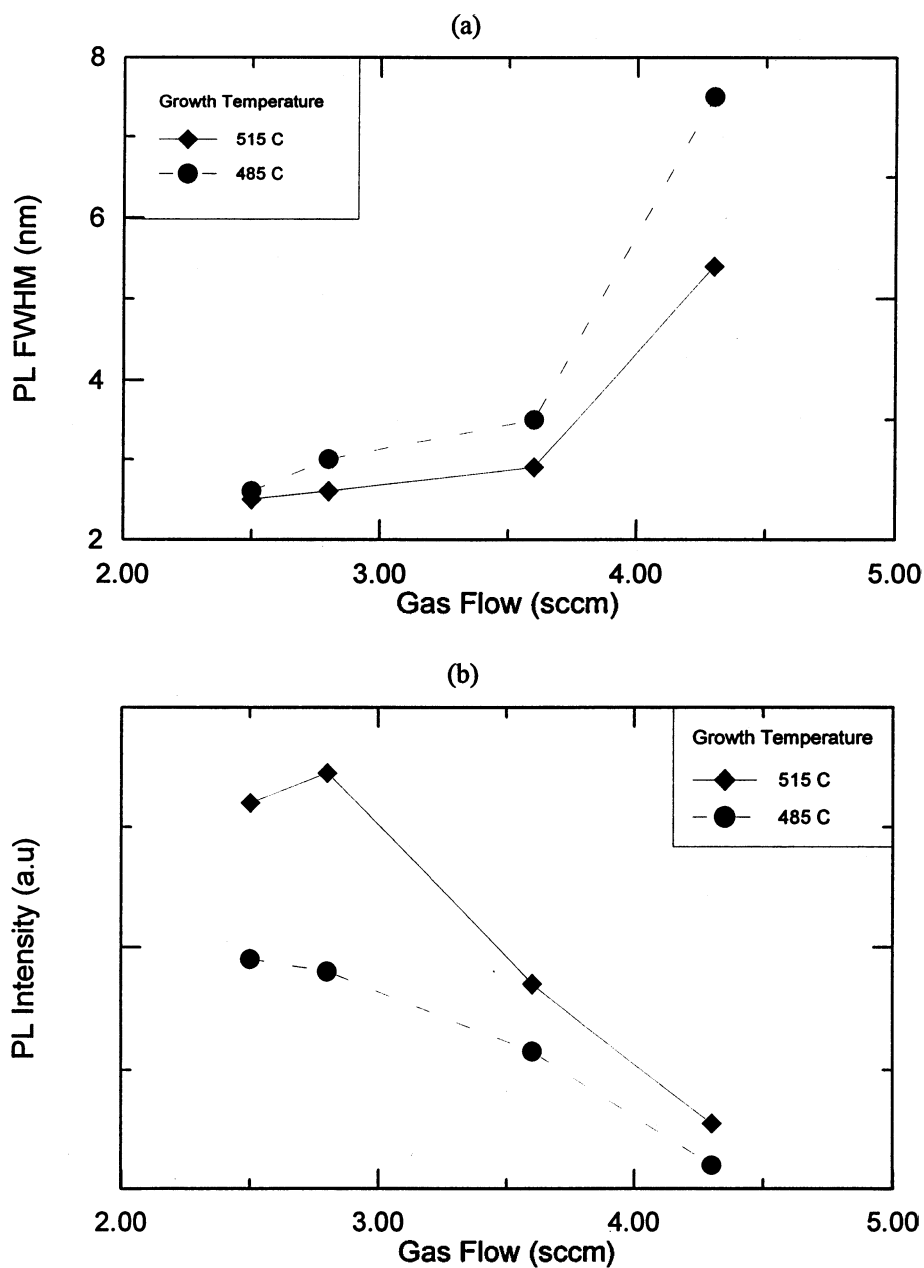


Fig. 4.4: PL spectra at 11K of samples in the group V flow rate study.

Figure 4.4 summarizes the PL results of the second study, where for both temperatures the structures grown with high flow rates have significantly wider FWHM and lower peak intensity. This finding is consistent with rough interfaces resulting from the lower migration length of the group III atoms on the growing surface due to the

higher group V overpressure. The results also show that the optical properties of the structures grown at 485°C are consistently worse than those grown at 515°C. Although it cannot be confirmed with any certainty, this may be due to the poor quality of GaAs grown at 485°C, which is far below the optimum growth temperature range of 580 to 650°C [4.2] for this material.

The studies conducted above indicate the QW's grown at 515°C with an AsH₃ flow rate of 2.8 sccm yield the best optical properties. It must be noted that although the optical properties of the QW's grown with the above conditions are good, a complete optimization the InGaAs/GaAs QW growth conditions has not been attempted. This material will, however, allow progress towards the goal of producing 980 nm lasers by comparing the PL results with results from broad area laser grown at similar conditions.

4.3 Broad Area Lasers

In this section the results for broad area lasers are presented. This part of the work was undertaken for two reasons. First, to quickly assess if significant improvement in material quality had been made since the first attempt at laser fabrication and second, to correlate the results of the QW PL study with actual device performance. For this purpose four identical laser layer structures were grown (see Figure 4.5) under different growth conditions. The growth conditions for the active regions of samples BAL4 and BAL2 were identical to the growth conditions for QW samples PL10 and PL6 (see Table 4.2).

GaAs	2000	$p > 10^{20}$
InGaP	5000	$p = 1 \times 10^{18}$
GaAs	1000	undoped
InGaAs	100	
GaAs	1000	undoped
InGaP	5000	$n = 1 \times 10^{18}$
GaAs	2000	$n = 2 \times 10^{18}$
GaAs Substrate		

Fig. 4.5: Structure grown for broad area laser study.

Sample #	AsH ₃ Flow Rate (sccm)	Growth Temp.
BAL1	2.8	530
BAL2	2.8	515
BAL3	2.8	500
BAL4	2.8	485

Table 4.3: QW growth conditions for broad area laser study.

The growth conditions for laser samples BAL3 and BAL1 were selected to further explore the growth conditions around sample PL6 which yielded the best optical characteristics in the QW study. The growth conditions for the active area of all four laser structures are summarized in Table 4.3. Following the growth, the four laser samples were fabricated into 50 μm wide stripe, broad area lasers. All four samples went through the fabrication process together in order to eliminate some of the process variations which may occur between different process runs. Each of the fabricated wafers were cleaved into 200, 300 and 500 μm cavity chips. Due to the low cleaving and mounting yield there was not enough material for a larger variety of cavity lengths. Samples were then mounted on copper heat sinks for testing under pulsed current conditions (0.2 μs pulse width and 10% duty cycle).

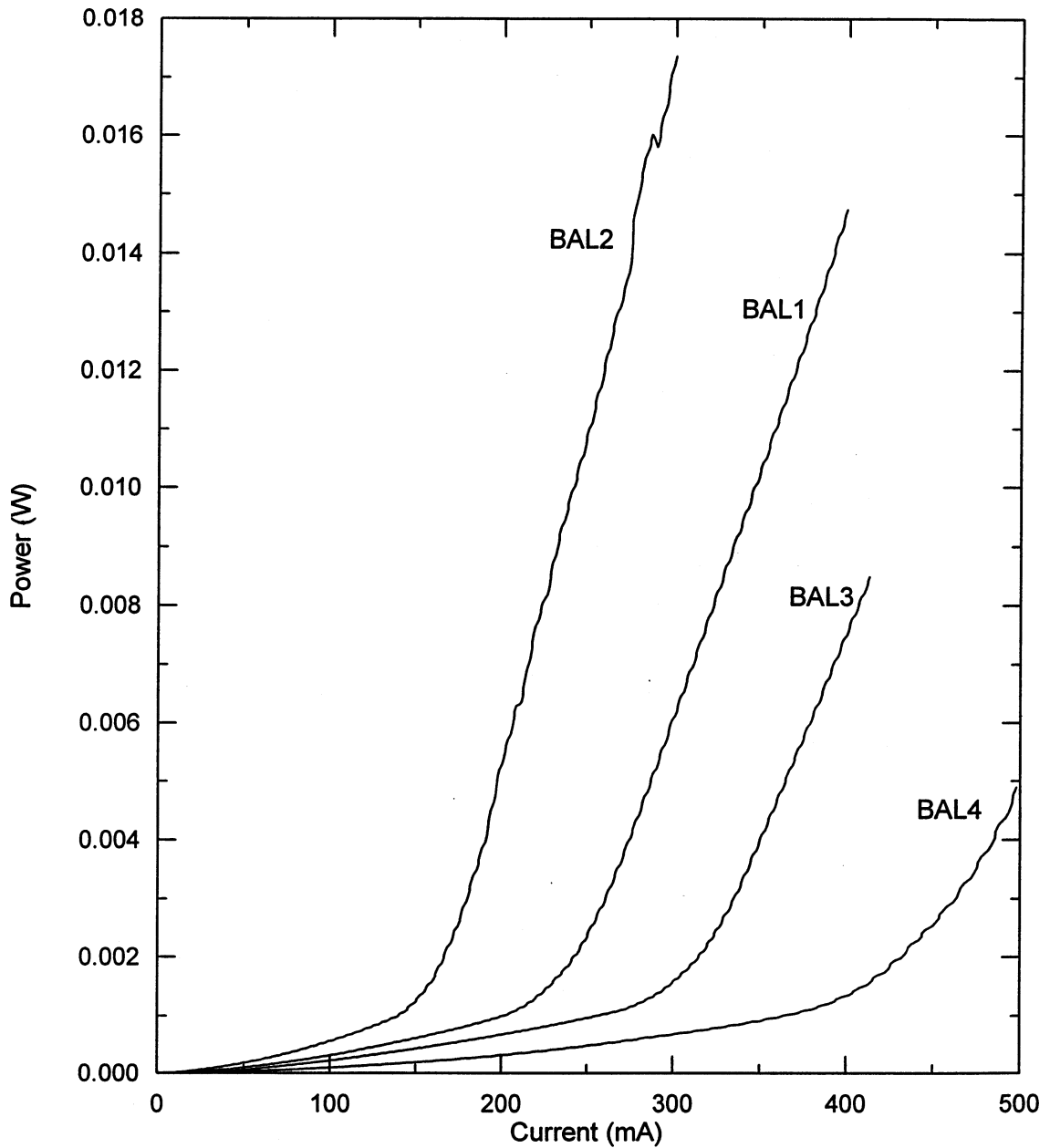


Fig. 4.6: Typical pulsed P-I plots for 50 x 500 μm broad area lasers.

Under these current injection conditions all the devices worked to varying degrees except for sample BAL4 where only the 500 μm cavity lasers worked. Typical P-I plots for the various 500 μm cavity lasers are shown in Figure 4.6. These results all show a significant improvement compared with the first set of laser devices shown in Figure 4.1.

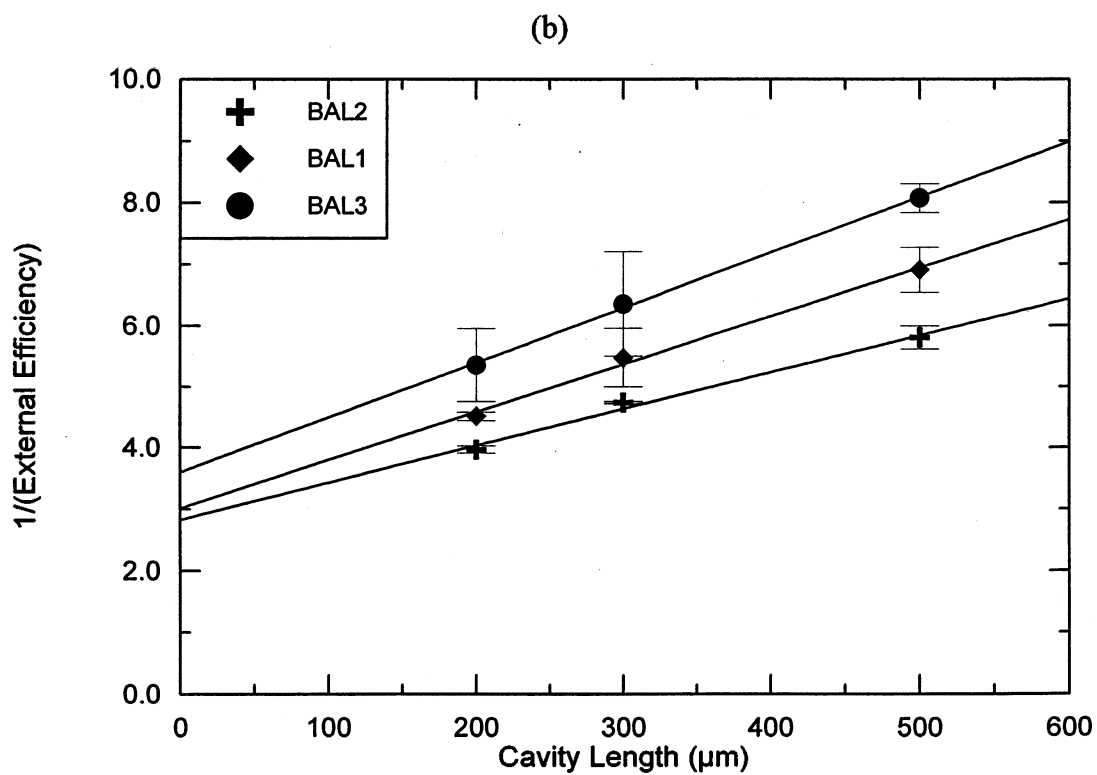
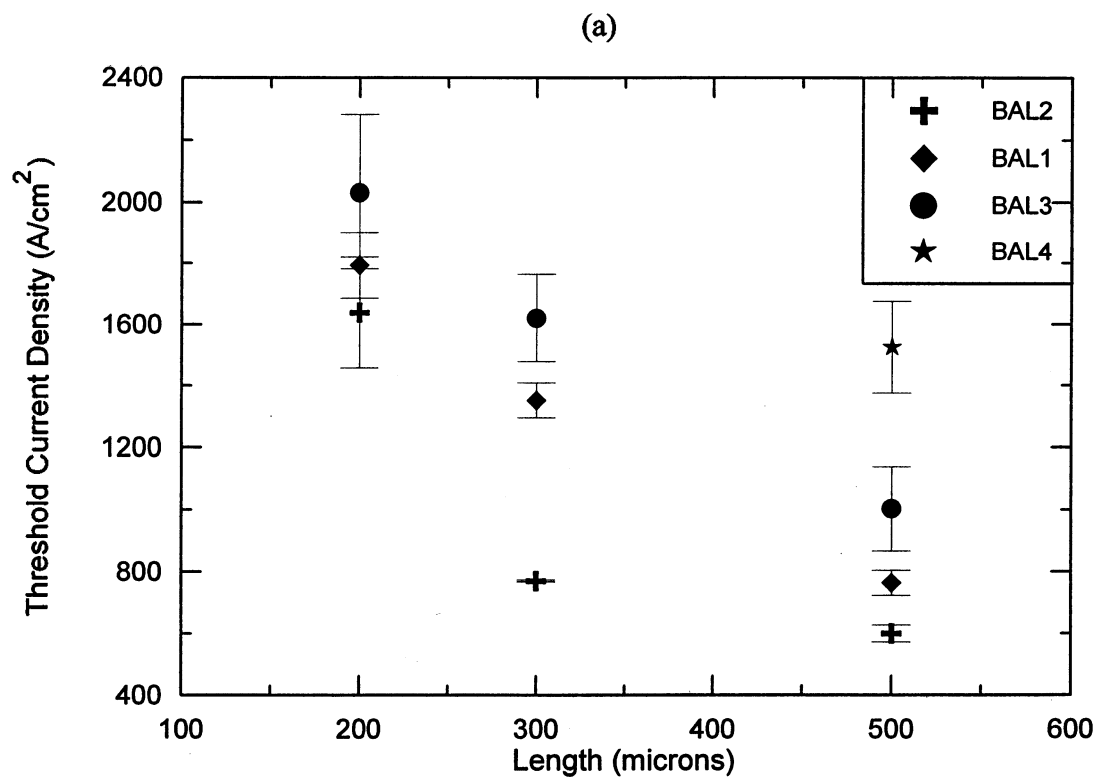


Fig. 4.7: Comparative analysis of 50 μm strip broad area lasers: (a) threshold current vs cavity length, (b) external quantum efficiency vs cavity length.

From the P-I data, threshold current densities (see Figure 4.7a) and external quantum efficiencies (see Figure 4.7b) were calculated for all the laser chips. From Figure 4.7b, the Internal Quantum Efficiency (IQE) and the cavity loss were determined as described in Section 2.3. These results are summarized in Table 4.4.

Growth #	IQE (%)	Cavity Loss (1/cm)
BAL1	35.39	30.74
BAL2	44.44	26.34
BAL3	32.41	32.63
BAL4	-	-

Table 4.4: Summary of broad area laser results

The values listed, in Table 4.4 were determined from a linear fit of three points with large associated errors. As such, the numbers are meant to indicate a trend rather than an absolute value. The trend shown by the results in Table 4.4 together with the threshold results in Figure 4.7a, clearly indicate that the growth conditions used for sample BAL2 yield the best laser characteristics. This agrees with the results of the PL study in section 4.2.

4.4 RWG Lasers

Using the growth conditions from sample BAL2 in the QW region, a new sample was grown to be used for the fabrication of ridge waveguide lasers. The layer structure is shown in Figure 4.8. This structure contains a thicker cladding layer as well as a GaAs etch stop to allow for the definition of the ridge waveguide. This structure was processed into 2 and 4 μm wide-ridge waveguide lasers with cavity lengths varying from 500 to 1500 μm .

GaAs	0.2 μm	$p > 10^{19}$
InGaP	1.5 μm	$p = 1 \times 10^{18}$
GaAs	10 nm	$p = 1 \times 10^{18}$
InGaP	0.3 μm	$p = 1 \times 10^{18}$
GaAs	0.1 μm	undoped
InGaAs	10 nm	undoped
GaAs	0.1 μm	undoped
InGaP	1.0 μm	$n = 1 \times 10^{18}$
GaAs	0.5 μm	$n = 2 \times 10^{18}$
Substrate		

Fig. 4.8: Layer Structure for ridge waveguide lasers.

Typical P-I plots for these devices are shown in Figure 4.9, where the devices were operated and tested CW. Furthermore, Figure 4.10 (b) plots $1/\text{EQE}$ (determined as shown in section 2.2) vs the cavity length, and Figure 4.10 (a) shows the threshold current density vs the cavity length. Each data point on the plot (see Figure 4.10) represents the average result from 12 separate devices. From this data the internal quantum efficiency and cavity loss were calculated. The results for the two ridge widths are summarized in Table 4.5.

Industrial quality lasers at this wavelength typically have an internal quantum efficiency of 90% and a cavity loss of 1.3 cm^{-1} [1.19]. The devices processed in this thesis compare well with this standard, considering the growth conditions are not fully optimized. This implies the processing procedure for these structures is reasonably satisfactory for device fabrication.

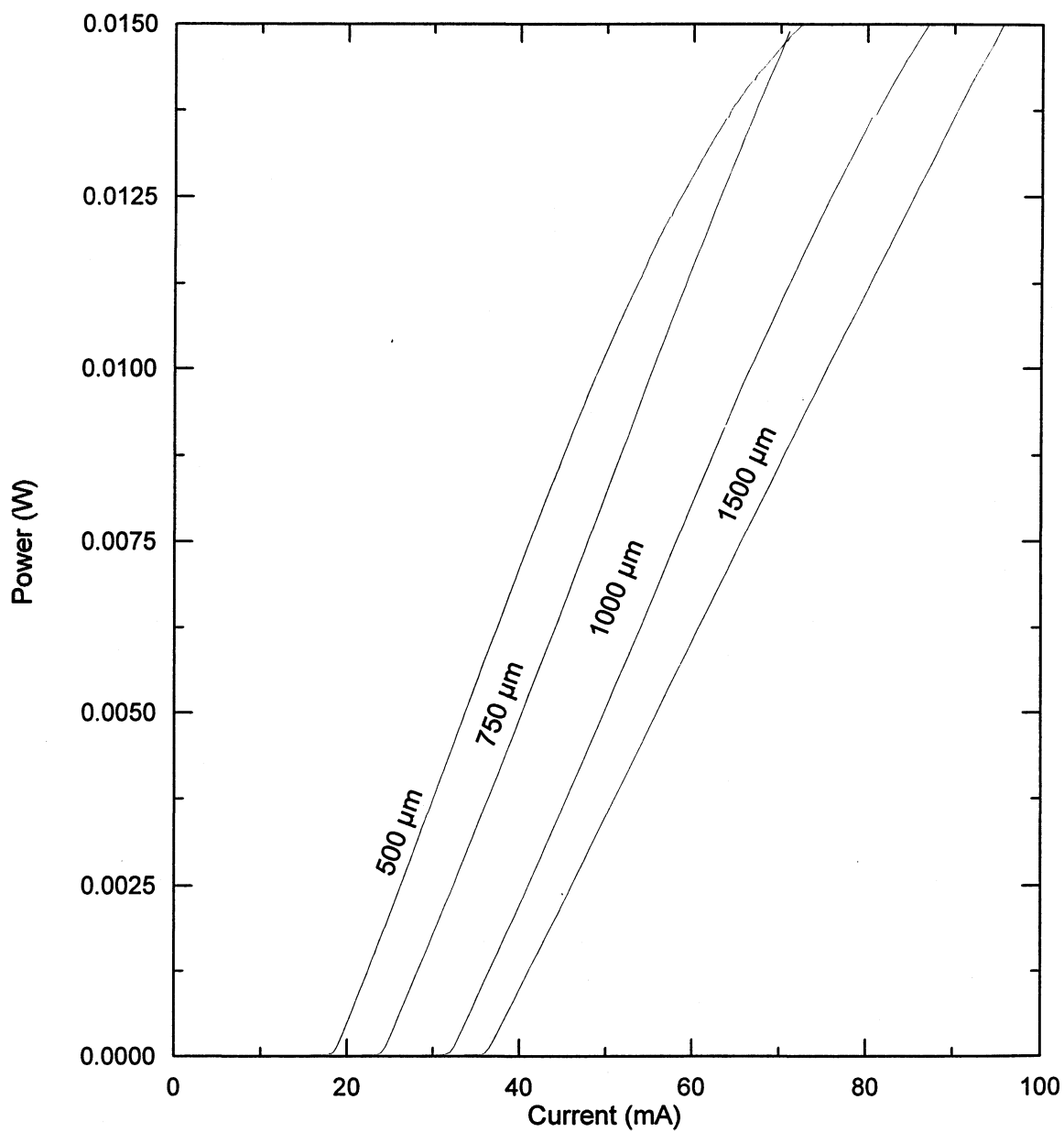


Fig. 4.9: Typical CW P-I plots for 2 μm ridge waveguide lasers with 500, 750, 1000, 1500 μm cavity lengths.

Ridge Width (μm)	Internal Quantum Efficiency	Cavity Loss (1/cm)
4	71%	5.2
2	68%	7.7

Table 4.5: Internal quantum efficiency and cavity loss for 2 and 4 μm RWG lasers.

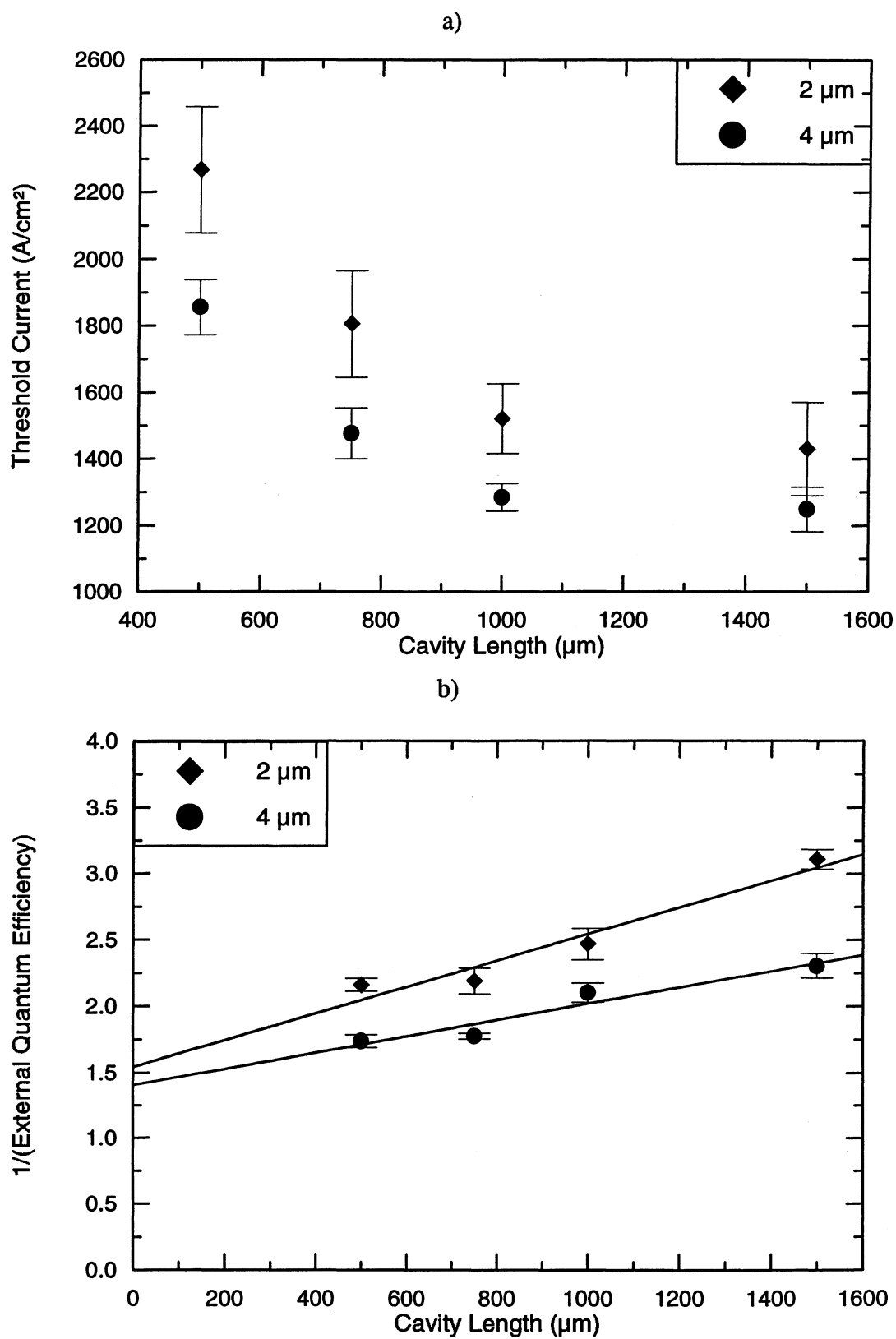


Fig. 4.10: Analysis of 2 and 4 μm ridge waveguide lasers: (a) threshold current vs cavity length, (b) inverse external quantum efficiency vs cavity length.

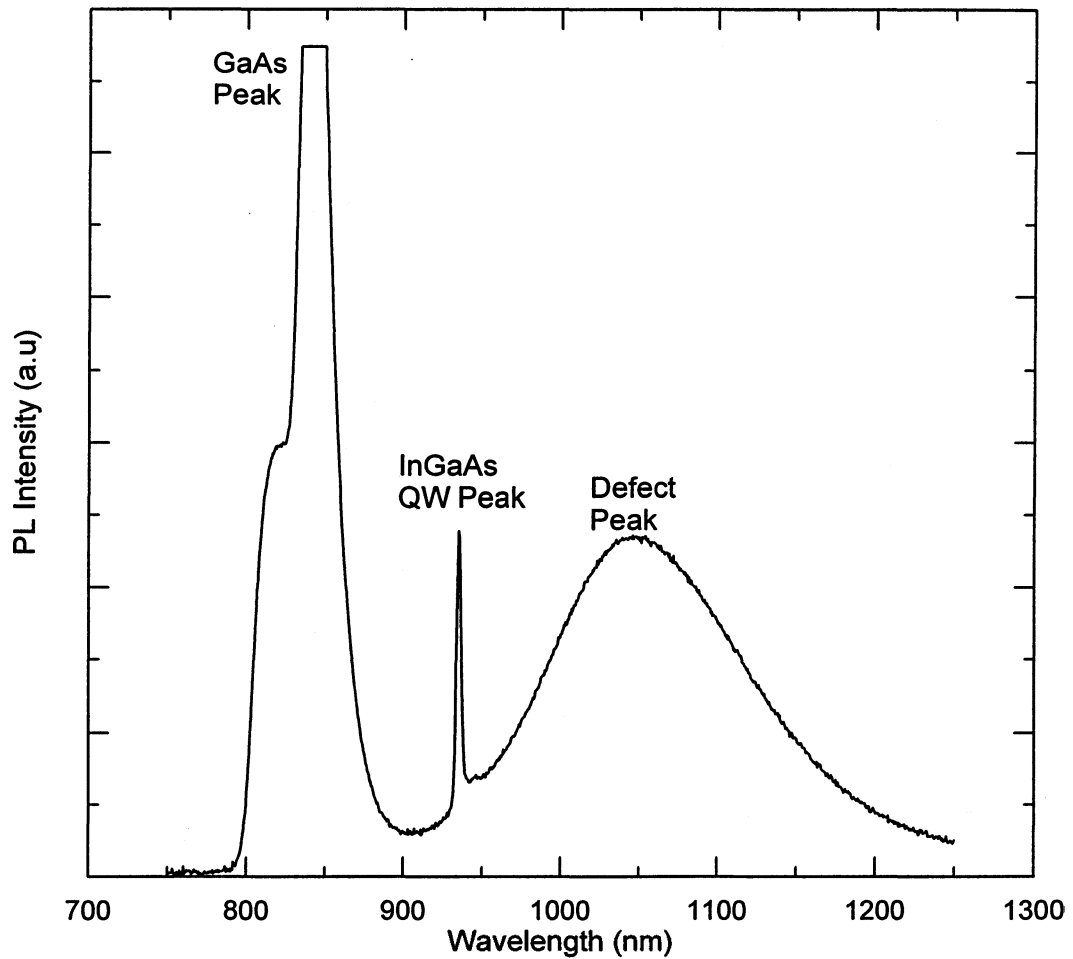


Fig. 4.11: PL spectra of ridge waveguide laser structure.

Photoluminescence of the RWG structure was used to check for any discrepancies which may give an indication of material or growth related problems. A typical PL plot is shown in Figure 4.11. A large, broad emission defect peak is clearly visible beginning around the energy of the emission from the active quantum well region. This defect peak will act to reduce the internal quantum efficiency of the laser by increasing the non-radiative electron-hole recombination rate. Also, the site may act as an absorption center increasing the cavity loss.

The above mentioned defect peak was not present in the photoluminescence spectrum of any of the QW samples grown in this thesis; nor was it present in the

photoluminescence spectrum of any of the bulk InGaP samples grown for growth calibration. These facts suggested that the defect may occur at the InGaP/GaAs interface. One possible cause of such a defect is the time delay at the GaAs/InGaP interface (about 2 minutes for the laser samples grown for this thesis) while the group V gases are being swapped. In order to investigate this possibility, six samples were grown (see Figure 4.12). Each sample contains three GaAs/InGaP interfaces labeled 1-3 in Figure 4.12, with gas swap time at interface 1 being set to five seconds for all the samples. The gas swap time at interfaces 2 and 3 was varied from 5 seconds to 2 minutes as shown in Table 4.6. The results of this study can be seen in Figure 4.13.

InGaP (lattice matched)	100 nm	undoped
Interface #3		
GaAs	200 nm	undoped
Interface #2		
InGaP (lattice matched)	100 nm	undoped
Interface #1		
GaAs	100 nm	undoped
Substrate		

Fig. 4.12: Structure for interface gas swap study.

Sample #	Gas Swap Delay Interface #1	Gas Swap Delay Interface #2	Gas Swap Delay Interface #3
PL12	5 secs.	2 mins.	2 mins.
PL13	5 secs.	5 secs.	5 secs.
PL14	5 secs.	25 secs.	25 secs.
PL15	5 secs.	2 mins.	5 secs.
PL16	5 secs.	5 secs.	2 mins.
PL17	5 secs.	80 secs.	80 secs.

Table 4.6: Gas swap delay times for the interface study.

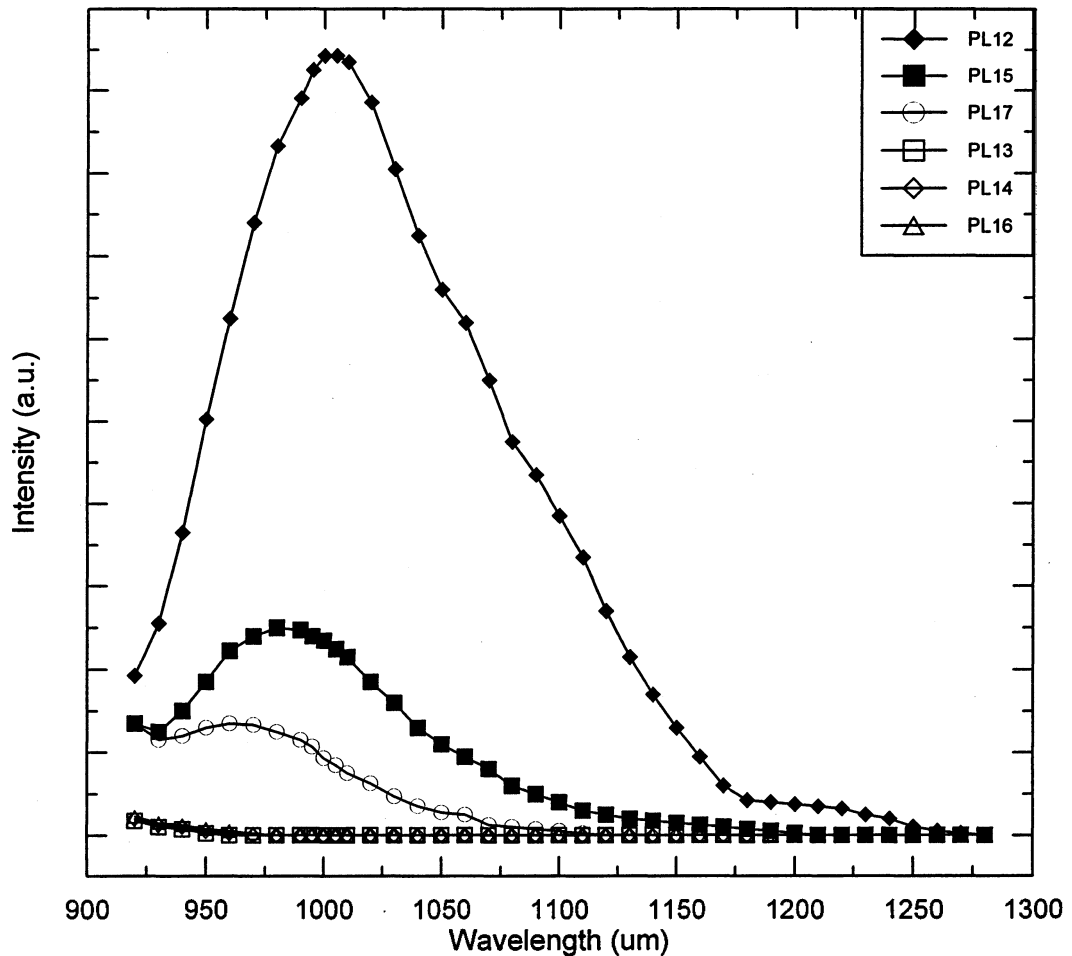


Fig. 4.13: PL spectra of the defect peaks for the interface study.

As seen in Figure 4.13 the defect peak only appears on the samples with long delay times on the second interface. This defect peak may be due to the formation of a thin InGaAs layer at the GaAs/InGaP interface. This small band gap material would trap carriers produced in the bulk layers where they would otherwise recombine. The trapped carriers could then radiatively recombine producing this broad peak. It is evident however that by using short gas swap times, at the GaAs/InGaP interface, for future 980nm RWG laser growths, significant improvements on the performance of these devices can be achieved.

5.0 CONCLUSION

In summary, the growth of 980nm QW lasers has been optimized. This was achieved by a series of experiments, the first of which addresses the issue of the difference in optimum growth temperatures for GaAs and InGaAs. It was determined that although their optimum bulk growth temperatures are approximately 100°C apart, the optical characteristics of the InGaAs/GaAs QWs are best when both materials are grown at the same temperature.

Following this finding, an attempt was made to determine the optimum group V flow rate, as well as to continue to assess the optimum growth temperature. Here, eight samples were grown at two different temperatures and four different flow rates. Looking at this set of growths, it was evident that the samples grown at 515°C demonstrated consistently better optical characteristics, for all four flow rates, than those grown at 485°C. In addition, it was clear that the optical characteristics of the QWs degraded as the flow rate increases for samples grown at both 515°C and 485°C. As a result the optimum growth condition was found to be 515°C substrate temperature and 2.8 sccm flow rate.

Further growth optimization was achieved via broad area laser characterization. This work entailed the growth of four samples with growth temperatures varying between 485°C and 530°C. The group V flow rate for all four samples was kept constant at 2.8 sccm. These devices were processed into broad area lasers and then tested. Analysis of

the results showed, that the devices grown at 515°C yielded the best device characteristics.

Subsequently, a RWG laser structure was grown, fabricated and tested. CW operation was achieved. The device showed internal quantum efficiencies of 71% and internal losses of 5.2/cm. Further PL analysis of this material revealed the presence of an unidentified defect peak in the wavelength regime of the InGaAs QW PL emission peak. This defect peak will act to reduce the internal quantum efficiency of the laser by increasing the non radiative electron-hole recombination rate. Also this defect site may act as an absorption center, thus increasing the cavity loss.

As shown in the last set of experiments, this defect peak was due to the long group V swap times at the InGaP/GaAs interface. Keeping the gas swap time down to approximately 5 seconds can completely eliminate the defect peak.

Future laser structures grown with low gas swap times should yield devices with higher efficiencies and lower cavity losses.

REFERENCES

- [1.1] R.G. Smart, J.L. Zyskind, and D.J. DiGiovanni: *IEEE Photon. Technol. Lett.*, **7**, 770-773, (1993).
- [1.2] J.L. Zyskind, C.R. Giles, J.R. Simpson, and D.J. DiGiovanni: *AT&T Tech. J.*, **71**, 53-62, (1992).
- [1.3] F. Fontana and G. Grasso: *Fiber and Integrated Optics*, **13**, 135-145, (1994).
- [1.4] T.R. Chen, L. Eng, B. Zhao, Y.H. Zhuang, S. Sanders, H. Morkoc, and A. Yariv: *IEEE J. Quantum Electron.*, **26**, 1183-1189, (1990).
- [1.5] J.M. Kuo, Y.K. Chen. and M.C. Wu: *Appl. Phys. Lett.*, **59**, 2781-2783, (1991).
- [1.6] P.L. Derry, H.E. Hager, K.C. Chiu, D.J. Booher, E.C. Miao, and C.S. Hong: *IEEE Photon. Technol. Lett.*, **4**, 1189-1191, (1992).
- [1.7] E. Desurvire: *IEEE Photon. Technol. Lett.*, **2**, 208-210, (1990).
- [1.8] J.C. Bean: "Materials and Technologies for High-Speed Devices", High-Speed Semiconductor Devices, S.M. Sze, Ed., Wiley, New York, (1990).
- [1.9] J.W. Matthews and A.E. Blakeslee: *J. Crystal Growth*, **27**, (1974).
- [1.10] H. Asai, and K.Oe.: *J. Appl. Phys.*, **54**, (1983).
- [1.11] R.M. Kolbas, N.G. Anderson, W.D. Laidig, Y.K. Sin, Y.C. Lo, K.Y. Hsieh, and Y.J. Yang: *IEEE J. Quantum Electron.*, **24**, (1988).
- [1.12] X.Z. Lu, R. Garuthara, S. Lee, and R.R. Alfano: *Appl. Phys. Lett.*, **52**, (1988).
- [1.13] J.J. Coleman: "Strained layer QW heterostructure lasers", Quantum Well Lasers, P.S. Zory, Ed., Academic, (1993).
- [1.14] S. Adachi: *J. Appl. Phys.*, **53**, (1982).
- [1.15] S.W. Corzine, R.H. Yan, and L. A. Coldren: "Optical Gain in III-V Bulk and Quantum Well Semiconductors", Quantum Well Lasers, P.S. Zory, Ed., Academic, (1993).

- [1.16] R.G. Waters: *Prog. Quant. Electr.*, **15**, (1992).
- [1.17] T. Yuasa, M. Ogawa, K. Endo, and H. Yonezu: *Appl. Phys. Lett.*, **32**, (1978).
- [1.18] S.L. Yellen, A.H. Shepard, C.M. Harding, J.A. Bauman, R.G. Waters, D.Z. Garbzov, V. Pjataev, V. Kochergin and P. Zory: *IEEE Photon Technol. Lett.*, **4**, (1992).
- [1.19] H. Asonen, A. Ovtchinnikov, G. Zhang, J. Nappi, P. Savolainen, and M. Pesa: *IEEE J. Quantum Electron.*, **30**, (1994).
- [1.20] C.T. Foxon, B.A. Joyce, M.T. Norris: *J. Cryst. Growth*, **49**, 132 (1980).
- [1.21] M.B. Panish, H. Temkin: "Gas Source Molecular Beam Epitaxy", Springer Series Vol. 26 Springer-Verlag Berlin Heidelberg (1993).
- [1.22] C.T. Foxon, M.R. Boudry, B.A. Joyce: *Surf. Sci.*, **44**, 69 (1974).
- [1.23] M.A. Herman, H. Sitter: "Molecular Beam Epitaxy", Springer Series Vol. 7 Springer-Verlag Berlin Heidelberg (1989).
- [1.24] G.W. Wicks: *Critical Rev. in Solid S. and Mater. Sc.*, **18**,239 (1993).
- [1.25] R.R. Lapierre: M.Eng. Thesis, Dept. of Engineering Physics, McMaster University (1994).
- [1.26] B.J. Robinson, D.A. Thompson, P.G. Hofstra, G. Balcaitis, and S.A. McMaster: Fourth International Conference on InP and Related Materials (1992).
- [2.1] S. Perkowitz: "Optical Characterization of Semiconductors", Academic Press New York (1993).
- [2.2] R.F. Pierret: "Advanced Semiconductor Fundamentals", Modular Series on Solid State Devices Vol. 6, Addison-Wesley Massachusetts (1989).
- [2.3] B. Mroziwicz, M. Bugajski, and W. Nakwaski: "Physics of Semiconductor Lasers", Amsterdam North Holland, (1991).
- [2.4] B.E.A. Saleh, M.C. Teich: "Fundamentals of Photonics", John Wiley and Sons New York (1991).
- [2.5] W.V. Roosbroeck and W. Shockley: *Phys. Rev.*, **94**, 1558 (1945).
- [2.6] J.I. Pankove: "Optical Processes in Semiconductors", Dover Public. New York (1975).

- [2.7] R.J. Elliot: *Phys. Rev.*, **108**, 1384 (1957).
- [2.8] T.P. Pearsall, L. Eaves, and J.C. Portal: *J. Appl. Phys.*, **54**, 1037 (1983).
- [2.9] E.F. Schubert and Tsang: *Phys. Rev.*, **34**, 2991 (1986).
- [2.10] H.A. Herman, D. Bimberg, and J. Christen: *J. Appl. Phys.*, **70**, R1, (1991).
- [2.11] G.P. Agrawal and N.K. Dutta: "Long-Wavelength Semiconductor Lasers", Van Nostrand Reinhold, New York (1986).
- [4.1] N. Chand and R.F. Karlicek Jr: "Epitaxy of InGaAs", Properties of Lattice Matched and Strained Indium Gallium Arsenide, P. Bhattacharya Ed., INSPEC (1993).
- [4.2] B. Hamilton and J.D. Medland: "PL Spectra of MBE GaAs", Properties of Gallium Arsenide, EMIS Group Ed., INSPEC (1986).
- [4.3] G. Zang, J. Nappi and M. Pessa: *Appl. Phys. Lett.*, **64**, 1009, (1994).